UNIVERSITY OF HELSINKI REPORT SERIES IN PHYSICS

HU-P-D257

Atomistic simulations of plasma-material interactions in fusion reactors

Elnaz Safi

Division of Materials Physics

Department of Physics

Faculty of Science

University of Helsinki
Helsinki, Finland

ACADEMIC DISSERTATION

To be presented, with the permission of the Faculty of Science of the University of Helsinki, for public criticism in auditorium XIII of the Main Building of the University of Helsinki, on March 3rd 2018, at 12 o'clock noon.

HELSINKI 2018

ISBN 978-951-51-4105-7 (printed version)
ISSN 0356-0961
Helsinki 2018
Unigrafia Print

ISBN 978-951-51-4106-4 (PDF version)
http://ethesis.helsinki.fi
Helsinki 2018
Electronic Publications @ University of Helsinki

Elnaz Safi, **Atomistic simulations of plasma-material interactions in fusion reactors**, University of Helsinki, 2018, 52 p. + appendices, University of Helsinki Report Series in Physics, HU-P-D257, ISSN 0356-0961, ISBN 978-951-51-4105-7 (printed version), ISBN 978-951-51-4106-4 (PDF version)

Abstract

With increasing demand for the energy in last decades, replacing scarce fossil fuels with new energy resources is inevitable. Currently, there is no clear alternative to the old and regular energy production methods for a clean future. However, nuclear fusion power may offer practical, power-plant-scale energy production with an unlimited fuel supply.

A major challenge to overcome in the fusion reaction is to produce more energy than it consumes under extremely harsh operating conditions. In the last few decades, a wide range of studies have been carried out to investigate fusion performance and fusion reactor designs.

ITER will be the first experimental tokamak-like nuclear fusion reactor to produce net energy, based on deuterium–tritium plasma. Due to the ITER design and operation requirements, extreme conditions are expected for plasma-facing components, such as very large thermal loads, temperature and particle fluxes. Therefore, selecting appropriate materials for different components of the device is critical and highly demanding.

The main candidates for the first wall materials in future fusion reactor, ITER are tungsten for the divertor plates and beryllium for the main wall. Moreover, special low-activation ferritic steels are developed for being used as structural materials in blanket modules. In addition, various steels containing of iron and carbon are being considered for the main wall of the DEMO.

The plasma cannot be confined infinitely and to control the contact between the escaped plasma and the wall, the area of interaction is restricted to divertor or limiter structures, leading to erosion of them. This phenomenon can become a show stopper by limiting the lifetime of wall materials. Therefore, characterizing the erosion behaviour and morphology changes of these components and understanding the underlying mechanism are essential toward predicting and ultimately controlling the adverse effects of plasma surface interactions.

Experiments in the different tokamaks and linear plasma devices, as well as those using ion beams are dedicated to study plasma surface interactions. However, experiments show a complex outcome and provide insufficient information to understand the underlying mechanism if the physics is poorly understood. In addition to experiments, computer simulations to study plasma surface interaction have also contributed to a better understanding of future fusion reactors and characterization of this mechanism in a wide range of time and length scales.

In this dissertation, the plasma wall interactions such as erosion and ion reflection for the first-wall materials of future fusion reactors have been studied by different computational methods. The interactions of different materials with plasma and impurity particles were modelled. The work was mainly based on molecular dynamics (MD) simulations and an Object Kinetic Monte

Carlo (OKMC) algorithm to extend earlier results to a longer time and length scales and thereby enables direct comparison with performed experiments.

First, deuterium irradiation on pure Fe, Fe with 1% C impurity and Fe_3C, under different irradiation energies and substrate temperatures was modelled. C preferential sputtering to Fe was reported, while D was found to be mainly trapped as D_2 in bubbles. Furthermore, a MD study to investigate the effect of plasma impurities D, Ar and Ne on the erosion and surface structure of W and Be was carried out for different fractions of Ar and Ne. In W, only noble gas impurities were responsible for surface erosion in the energy range studied here, and the sputtering mechanism was physical. For Be at impact energies higher than 100eV, the total Be sputtering yield in the presence of Ar and Ne impurities was found to be three times higher than for pure deuterium irradiation. The effect of surface temperature on the results was negligible.

Furthermore, the effect of reactor-relevant parameters on Be erosion behaviour and surface changes have been investigated using MD and subsequently a multi-scale approach (KMC-MD). This study gave us a better understanding of the erosion mechanism and improved the knowledge of molecular erosion and its underlying structure. Moreover, this approach was able to offer a more precise database of erosion yields to the large-scale-impurity-transport codes such as ERO. The findings correlate well with different experiments performed at the JET and PISCES-B devices.

Contents

Chapter 1

Introduction

One of the most important challenges of the 21^{st} century is to develop new energy resources that can fulfil the increasing demand for energy caused by the current population growth. The primary energy sources and fossil fuels such as coal, heavy crude oil and natural gas are becoming scarce [1] and their extraction becoming questionable from the economics point of view, therefore, new energy resources must replace them. In addition, these primary energy sources emit the green-house gas (CO_2), which could affect the atmosphere and increase the global warming and climate change [2]. During the last decades, a few reliable and clean solutions as alternatives to fossil fuels have been under development; these include wind, solar and hydropower energies. On the one hand, these renewable energy sources are greatly progressing for a safe and CO_2-free future, and on the other hand, their efficiency highly depends on the geographical location and climate conditions [3].

Nuclear fusion may offer a power plant scale energy production with an almost unlimited fuel supply. It is safe, has no emission of harmful gases, no long lived radioactive waste and it is independent from local weather and geographical conditions. Fusion is a process where large amount of energy is produced by the same process that happens in stars. In fusion, light atoms fuse into new heavier elements that release the excess binding energy as heat. The most suitable fusion reaction for an earthbound fusion is between two hydrogen (H) isotopes, deuterium (D) and tritium (T). When these two D and T nuclei fuse together (Fig. 1.1), on one hand, they form a neutron (n) with an energy of 14.1 MeV. Later, this hot neutron is captured, and its energy can be used just as in a conventional power plant; e.g. to heat a coolant fluid (e.g. water) for producing steam to run a turbine. On the other hand, a helium nucleus (He) with an energy of 3.5 MeV is produced. Since the helium nuclei are charged, they will stay inside the fusion reactor and transfer their energy to the plasma, keeping it hot. Another benefit of fusion is the abundancy of its fuel components in the earth: about 33 g of D is available in every cubic metre of sea water and T can be generated from lithium (Li), which is a common element in the earth's crust. Further, the fusion reaction is very efficient and a very large amount of energy is produced only by consuming a small amount of fuel; 250 kg of fuel could run a D-T fusion power plant for a year [4].

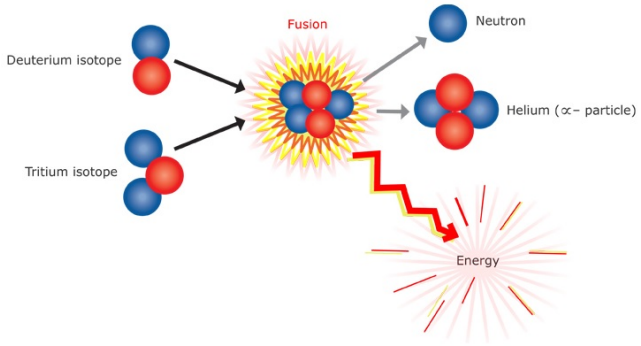

Figure 1.1: D-T fusion [5]. the fusion of deuterium with tritium creates helium^4, frees a remaining neutron, and releases energy. Because $E = \Delta MC^2$, when two atoms are fused, a very small amount of mass can be converted into a large amount of energy.

In thermonuclear fusion, the nuclei must be forced together in spite of repulsive electrostatic Coulomb force, by heating the fuel up to temperatures around 200 million degrees, for the D+T reaction. At these temperatures atoms are highly ionized and form a plasma. The primary requirements for fusion reaction are very precise and the process could easily stop if these requirements are not met during the process. This is the main reason why there is no fusion reactor up to this date which can produce more energy than it consumes. So far, the highest energy gain factor (Q) was reached at the Joint European Torus (JET), the largest fusion reactor in the world, with Q = 0.64 in 1997 [6]. The power output is maximized by controlling essential plasma parameters, such as the confinement time, the density and the temperature, which cause major challenges. For this purpose different fusion devices have been developed, while the most favourable and promising one is the *tokamak*.

In a tokamak reactor, the plasma is confined by combining poloidal and toroidal magnetic field and isolated by a twisted-torus shaped vacuum vessel [7]. Due to finite plasma confinement, particles can escape from the core and either hit the surrounding wall or join to other impurities and He nuclei in the exhaust region, called *divertor*. The plasma will interact with the inner surrounding walls of the reactor, the plasma facing components (PFCs). The PFCs include the main wall and the divertor. These plasma wall interactions (PWIs) can harm both the wall and the plasma. The wall gets thinner due to erosion. If the eroded particles migrate to the confined plasma, they will cause energy loss by radiation. Radiation losses depend on the atomic number of the impurity (Z) where heavier elements are more harmful [8]. Moreover, controlling the erosion is important to maximize the lifetime of wall materials.

The choice of materials exposed to plasma particles is critical to provide safe operation of the reactor and to be economically reasonable [9]. Examples of suitable plasma facing materials (PFMs) are tungsten (W) for the divertor region and beryllium (Be) for the first wall. W is selected because of its high sputtering threshold and low fuel retention [10]. Moreover, W has good power-handling capabilities due to its high melting point, however, it is a heavy (high-Z) material and so its erosion must be controlled. Be is a low-Z material which has been chosen due to its low plasma contamination, fuel retention and its oxygen gettering properties [11]. Nevertheless, Be is only suitable to use in areas with lowest heat loads and weakest plasma-

surface interactions (PSIs) due to its low sputtering energy threshold. Moreover, the material damage will be beyond the tokamak first wall and divertor, since the energetic particles can penetrate into the tokamak's blanket area which is mainly made of high-strength copper and stainless steel. Special low-activation ferritic steels are developed for being used as structural materials in blanket modules.

The behaviour of these materials in a reactor can be studied with experimental fusion devices. The road-map towards a future fusion power plant is built based in various devices. Due to their main wall material choice, the most relevant devices for the present work are: JET, its successor ITER (see Fig 1.2) and a demonstration reactor called DEMO. JET represents a pure scientific experiment aiming to test different materials and plasma configurations for ITER. The reactor scale experiment ITER is designed to deliver ten times the power it consumes, demonstrating that heat ignition can be achieved. The next foreseen device, DEMO, is expected to be the first fusion power plant to prove that production of net electricity in the grid is possible [12].

However, plasma parameters and desired conditions for a full-scale power plant cannot be reproduced in current experimental facilities and a complete experimental device is difficult to reach. Computer simulations techniques, such as those used in this thesis are required to provide a better insight on the experimental results, to achieve a theoretical conception of the experimental systems, and to predict the following steps more accurately. Further, it provides a better understanding of the behaviour of materials in a future fusion reactor and facilitates the development of a specific material.

The present thesis focuses on PWIs happening and expected in the fusion reactor main wall and vacuum vessel. These results will provide more accurate data for further plasma-wall interaction studies, and will help in the interpretation of experiments.

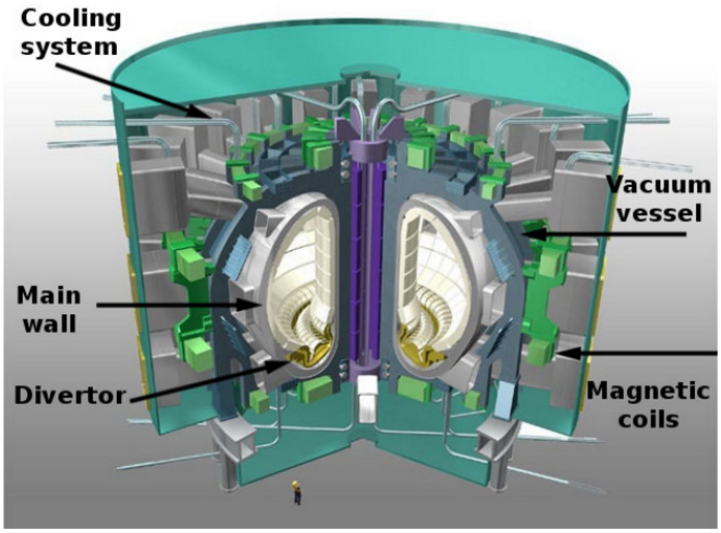

Figure 1.2: Next-generation fusion reactor ITER tokamak with plasma volume of 840 cubic meters and energy gain factor of 10 which produces 500 MW energy for a pulse of 100 seconds. [7].

Chapter 2

Purpose and Structure

The purpose of this thesis is to study the surface phenomena of main wall materials in a fusion reactor when subjected to energetic plasma particles. The developed models and the outcome will help better understanding of the experiments and also will provide a more precise and essential database for larger scale plasma-wall interaction models.

This thesis consists of a brief summary and four original articles, already published or accepted for publication in international peer-review journals. The publications are given in the appendix and referred to with bold Roman numbers in the text.

The structure of this thesis is as follows. In the present section, the articles are summarized and the author's contribution to each of them is explained. In section 3, the basic concepts of fusion reactor and plasma-surface interactions are described. All methods and models used in this thesis are described in section 4. Sections 5, 6 and 7 summarize the main outcomes of the thesis. In section 8 the work is summarized and the acknowledgement and references are found afterwards. At the end, the publications this thesis is based on are attached.

2.1 Summaries of the original publications

Publication I: Atomistic simulations of deuterium irradiation on iron-based alloys in future fusion reactors
E. Safi, J. Polvi, A. Lasa and K. Nordlund, *Nuclear Materials and Energy* **9**, 571-575 (2016)

> In this study, surface erosion and morphology changes of Iron-based alloys were investigated under D ion irradiation by molecular dynamics (MD) simulations. This study helped in predicting the life-time and viability of reactors with steel walls. In the presence of carbon (C), C sputtering was preferential to iron (Fe) and the surface was enriched with Fe. In general, our results revealed that if steels are used as a plasma-facing material, the presence of C in them will result in chemical sputtering of carbon-containing molecules.

Publication II: Plasma impurity co-bombardment effects on sputtering of beryllium and tungsten
E. Safi, A. Zitting and K. Nordlund, *Nuclear Materials and Energy* **9**, 571-575 (2016)

The main candidates of ITER plasma-facing materials are W and Be. Ions from the plasma as well as injected noble gas impurities such as Ar and Ne that are used as a coolant in the plasma, will lead to erosion of the wall materials. In this study, the effect of D, Ar and Ne impurities on W and Be sputtering and surface morphology changes were carried out by MD simulations. We modelled irradiation of both W and Be surfaces under a different mixture of Ar-D and Ne-D. In W, only Ar and Ne were responsible for surface erosion in the energy range studied here, and the sputtering mechanism was in the physical region. A blistering-like effect was observed due to D_2 accumulation in the Be cells at higher energies. We found that W and Be surfaces were more damaged at higher impurities concentration.

Publication III: Atomistic simulations of the effect of reactor-relevant parameters on Be sputtering
E. Safi, C. Björkas, A. Lasa, K. Nordlund, I. Sukuba and M. Probst, *Journal of Nuclear Materials* **463**, 805-809 (2015)

One of the best candidate for the first wall material in the present day fusion reactor, JET, as well as in ITER, is Be. Be will inevitably erode when being exposed to plasma particles such as D. Knowing the sputtering characteristics of the Be-D system is of vital importance. The aim of this study was to use MD techniques to gain insight into the effect of irradiation energy, particle flux and substrate temperatures on Be erosion. Special attention was paid to BeD_n molecules. The erosion behaviour of Be was found to be strongly dependent on D concentration at the surface.

Publication IV: Multi-scale modelling to relate beryllium surface temperature, deuterium concentration and erosion in fusion reactor environment
E. Safi, G. Valles, A. Lasa and K. Nordlund, *Journal of Physics D: Applied Physics* **50**, 204003 (2017)

In this study, we continued the same topic as in publication III, our previous study, MD modeling of cumulative D impacts on Be show a complex outcome for molecular erosion. Due to very different D profiles at different surface temperatures (T_{surf}), larger Be-D molecules were also emitted when the D concentration (C_D) increases on the topmost layer. In this work, more accurate beryllium deuteride (Be-D) molecular erosion yields, were computed in a MD - Object Kinetic Monte Carlo (OKMC) multi-scale approach, to appropriately account for the complex relationship between T_{surf} and C_D. First, we calculated the complex relationship between T_{surf} and C_D precisely by simulating the time evolution of the system

using an OKMC technique. These simulations provide a C_D profile for any T_{surf} and incoming D energy. We then describe how this profile can be implemented as a starting configuration in MD simulations. We finally used MD simulations to investigate the effect of temperature and impact energy on the erosion of Be due to D plasma irradiation. Increasing the surface temperature leads to a lower C_D at the surface, because of the tendency of D atoms to avoid being accommodated in a vacancy, and de-trap from impurity sites and diffuse fast toward bulk. At the next step, total and molecular Be erosion yields due to D irradiation were analyzed using MD simulations.

2.2 Author's contribution

The author of this thesis performed all MD simulations, as well as BCA tests of publication **I**, and wrote the entire manuscript. Technical set-up for part of the MD simulations was suggested by Dr. J. Polvi.

The author supervised and also performed half of the simulations by herself in publication **II** and wrote most of the publication.

In publication **III**, the author carried out most of the simulations and analysis, guided by Dr. A. Lasa, and wrote most of the publication.

The MD and OKMC simulations and analysis presented in and writing of publication **IV** were done entirely by the author. The OKMC set-up was guided by and extensively discussed with Dr. G. Valles.

2.3 Other publications with the author's contribution

In addition, the author, Elnaz Safi, has contributed in the MD simulations and manuscripts writing of the following publications, which, however, are not part of this thesis:

The relationship between gross and net erosion of beryllium at elevated temperature
R. P. Doerner, I. Jepu, D. Nishijima, E. Safi, L. Bukonte, A. Lasa, K. Nordlund and T. Schwarz-Selinger, *Journal of Nuclear Materials* **463**, 777-780 (2015)

Temperature dependence of underdense nanostructure formation in tungsten under helium irradiation
G. Valles, I. Martin-Bragado, K. Nordlund, A. Lasa, C. Bjorkas, E. Safi, J. M. Perlado and A. Rivera, *Journal of Nuclear Materials* **490**, 108-114 (2017)

Molecular dynamics simulations of helium bubble growth in tungsten
T. Bilyk, C. Björkas, E. Safi and K. Nordlund , *Journal of Nuclear Materials* **Submitted for publication** (2017)

Chapter 3

Plasma-material interactions

Plasma-material interaction (PMI) effects are among the most important problems to be solved along the way towards fusion as a reliable energy source. PMI issues in fusion devices are expected to have a strong impact on plasma performance, and affect the operation of devices as well as the choice of plasma-facing materials (PFMs)[13].

3.1 Thermonuclear fusion

Thermonuclear fusion is the main source of energy in the universe, as it is the energy source of stars. Fusion energy is generated in the sun when the nuclei of light elements, such as hydrogen, fuse together to form heavier elements. As given by Einstein's famous formula, $E = \Delta mc^2$, energy (E) is gained because of the change in the nucleus mass (Δm), where c is the speed of light.

However, because of the strong Coulomb repulsion of the nuclei, fusion reactions happen at high temperatures. The nuclei collide at high kinetic energies and a small fraction of them fuse together in a plasma environment, releasing a large amount of energy. For example, this is the reaction of choice in ITER:

$$^2D + ^3T \rightarrow n + ^4He + 17.6MeV. \tag{3.1}$$

Due to momentum conservation, most (80%) of the energy of the D-T fusion is carried away by neutrons (n). Some of these neutrons can be trapped in a blanket containing lithium (Li), leading to

$$^6Li + n \rightarrow ^3T + ^4He + 4.78MeV. \tag{3.2}$$

These reactions are the easiest ones to achieve so far [14]. According to these reactions, ^2D and ^6Li are the ultimate fuels for fusion. Since the fusion reaction is not a chain reaction, a fusion reactor is safe from nuclear explosion and the life time of the radioactive component, T, is short, 12.3 years.

3.2 Tokamak-like fusion reactors

Since the plasma particles are ionized, the plasma can be confined in a suitable toroidally closed magnetic surfaces [15]. The most developed design for plasma magnetic confinement is the tokamak. This method is also the basis for the design of near future fusion reactors. Figure 1.2 illustrates the tokamak configuration, where the plasma is surrounded by different walls. This magnetic system consists of superconducting toroidal and poloidal field coils, a central solenoid and a set of correction coils that magnetically confine, shape and control the plasma inside a vacuum vessel [16]. In order to prevent the entry of impurities from the air outside and the escape of the fuel from inside the chamber, as well as to protect the magnetic coils, the vessel of a tokamak is vacuum-proof. Moreover, the volume of the fusion plasma is determined by the size of the vacuum vessel; the larger the vessel, the greater amount of power can be produced. The interior surface of the vacuum vessel in ITER will be covered by a Li blanket, where part of the fuel is produced.

The limiter is a material surface within the tokamak vessel which defines the edge of the plasma and therefore avoids contact between the plasma and the vessel by limiting the plasma edge interactions with the main wall. The divertor is also a separate region in the reactor, where the exhausted ions leave the reactor. Both components are necessary for the tokamak-like fusion reactors [17].

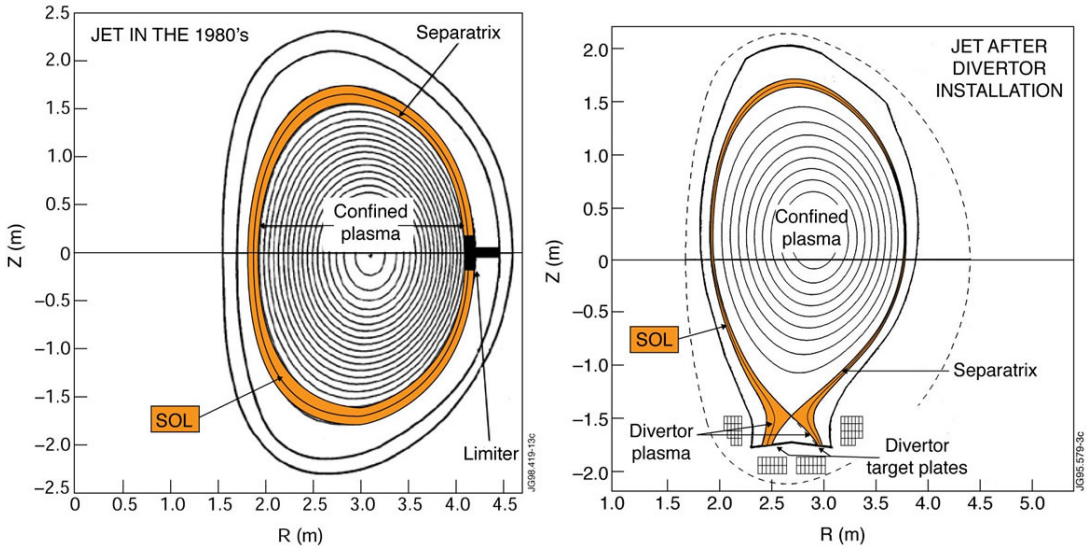

Figure 3.1: The cross section of JET tokamak, left: with only limiter at 1980's and right: with current limiter and after divertor installation. Courtesy of EFDA.

Figure 3.1 illustrates the cross section of JET tokamak with a limiter, before and after divertor installation. The plasma in the tokamak is divided into different regions. The core plasma is the area where the atoms fuse and the plasma is confined in closed magnetic field lines, where extremely high temperature and high plasma densities are needed [18]. The edge plasma is

cooler, while the hotter plasma is at the center; limiter and divertor materials are exposed to the edge plasma. The plasma that escapes the closed magnetic field lines is called exhaust and the last flux surface that separates the closed field lines of the core plasma from the open ones of the edge plasma is the *separatrix*. The part of the edge plasma where particles will penetrate radially during their journey from the separatrix towards the walls is the *scrape off layer* (SOL). The SOL transports most of the exhaust to the divertor plates along the field lines [19].

The tokamak main wall and limiter components are mostly eroded in the limiter phase of the plasma; in current tokamaks with Be main wall and limiters, and future tokamaks with possibly Fe-based alloys main wall and limiters. In addition, these eroded particles with other impurities together with high deuterium flux will be transported to and irradiate the divertor surface.

The erosion of PFCs can become a show-stopper by limiting the life time of components. Thus, choosing a proper material for divertor and limiter in future fusion reactor is highly critical. ITER was originally planned to begin operations with a divertor target made of carbon fiber-reinforced carbon composite (CFC). CFC is a material that has high thermal conductivity. However, the CFC has recently been discarded as the divertor material due to excessive fuel retention (see section 3.3). Thereafter, the interests returned to using full metallic first wall, mainly W and Be. In 2011, JET started operating ITER-like wall (ILW), with Be for first wall material and W for divertor region [20]. The similar decision has been done for ITER to explore the full high-Z material configuration and Fe-based alloys for DEMO.

3.3 Nature of plasma-wall interaction

Plasma-wall interactions (PWIs) are among the most important challenges along the way to construct the future fusion reactor. In a fusion reactor, a very hot plasma ($\approx$ 200 million degrees Celsius) is kept away from the wall of the chamber by using a strong magnetic field. However, this confinement cannot be perfect and the exhausted particles leave the reactor. Thus, the ions from the edge plasma will hit the PFCs. These interactions may cause problems as they involve high heat and particle fluxes from plasma. Therefore, the best candidates for PFMs are ones that are heat-resistant, thermally conductive, resistant to physical and chemical erosion, and show low fuel retention.

These three crucial issues are the main PWI concerns [21] :
1. Life time of PFMs.
2. Dust production from eroded PFMs.
3. Tritium(T) inventory in the vacuum vessel.

The PFMs may erode because of sputtering, melting, sublimation and brittle destruction [22]. The damage to the wall materials is caused by the impact of plasma fluxes and erosion of materials. This results in both reduction of material lifetime and plasma contamination. Figure 3.2 illustrates the main processes that happen at the plasma-surface interface and divertor plates. Details about different types of interactions existing at the first wall and divertor plates, as well as surface effects in PFMs, are discussed in the following paragraphs.

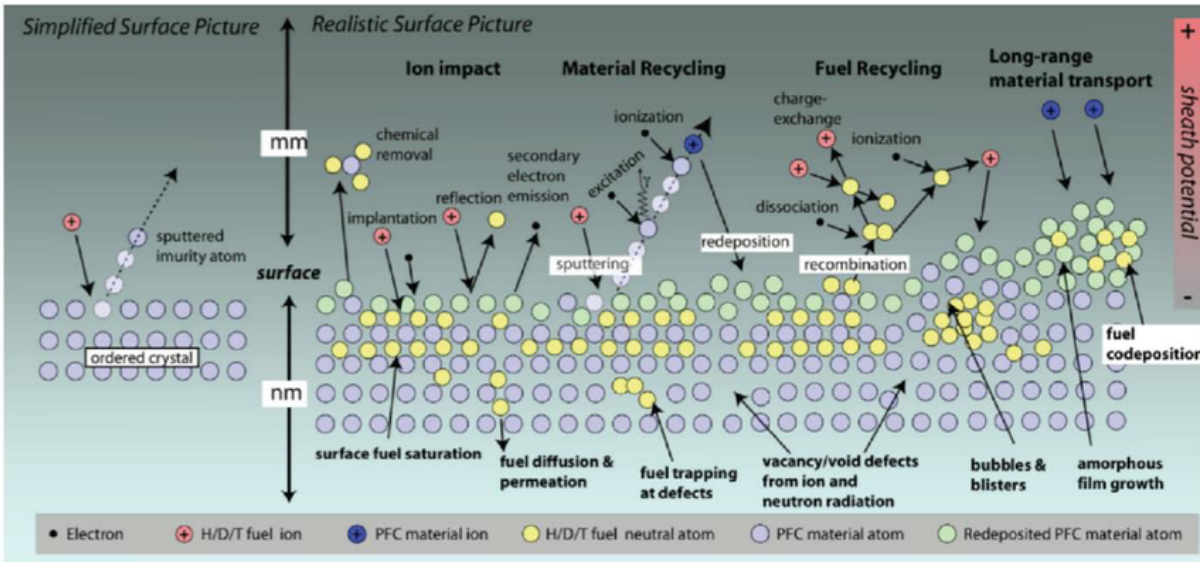

Figure 3.2: Schematic of complex plasma-surface interactions involving hydrogen (H), deuterium (D), tritium (T), and gamma ray (γ) interactions with near-surface lattice atoms. Image reproduced from [23]

In fusion science, dust particles will mainly result from erosion of thick deposits or damaged wall components which are due to PWI processes. Dust is particles in the nanometer (nm) or micrometer (μm) size range inside the vacuum vessel. Dust particles can result from various erosion processes. Also the size of dust particles is important. Some of them are too heavy to be moved by the plasma and tend to remain at the bottom of the vacuum vessel. They can be removed by vacuum chamber cleaning during the shutdown period. In contrast, smaller dust particles usually have a high sticking coefficient and make the cleaning procedure harder. Since C is not a component of the divertor anymore, dust production plays a relatively minor role in fusion devices and it seems not to be an operation hazard in comparison with the two other PWI issues [24].

Fuel retention is called to the fuel particle deposition or implantation in the PFCs. Retention becomes more important when radioactive tritium (T) is used as the fuel. For safety reasons, only a limited amount of the T will be allowed in fusion reactors. For example, the limitation for tritium content in ITER is 700 grams between shutdowns and this T retention level would be reached roughly after 1000 pulses with a duration of $\approx$ 1000 s. . Figure 3.3 shows the estimation of tritium retention in ITER for the all-C (blue line) and all-W options (red line) compared to the initial material choice CFC/W/Be (magenta). In addition, retention values for the option of a full-W divertor and Be first wall are included (black line). The assessment was performed assuming different particle fluxes to different divertor and wall areas [25]. It is also economically nonviable to retain the fuel on the wall, where it is unavailable to the burning plasma.

There are different mechanisms for T retention, such as co-deposition or implantation as shown in figure 3.2. Co-deposition is the simultaneous deposition of fusion fuel and impurity particles on the surface of the PFCs. Co-deposition of T with materials that eroded from PFCs is expected to be the main process of T accumulation in the vessel. Tritium can move deep inside the walls and be trapped in remote areas, which can make dust removal harder. For example,

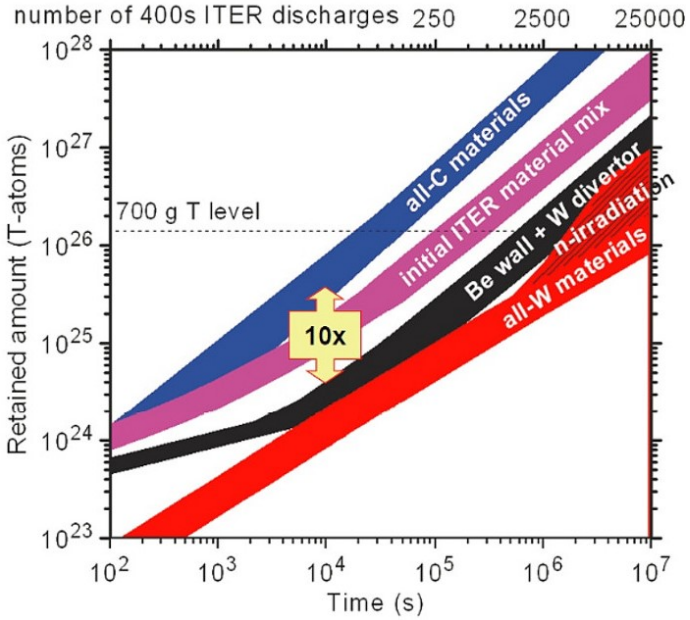

Figure 3.3: Estimation of in-vessel tritium retention in ITER for different plasma-facing materials. Image reproduced from[21]

the erosion of carbon leads to the production of hydrocarbons and eventually results in their re-deposition on the wall and in remote areas by trapping T. Co-deposition also occurs when Be is used as the main wall of the reactor.
T retention also happens by implantation mechanism where ions can go through the material and implant there.

3.4 Ion irradiation of materials

In this section, the interaction of edge plasma with wall components is explained. PWIs consist of all kind of interactions between particles coming from plasma, such as high energy neutrons or hydrogen, with every component of a reactor such as main wall components, breeding blanket and structural materials. Both surface and bulk effects can occur in components due to these interactions. However, the present thesis focuses on plasma surface interactions (PSIs) in atomistic level that happen in the first wall of the reactor and the divertor region.

3.4.1 Nuclear stopping

When a bombarding ion enters a target, it experiences a series of collisions with target atoms until the ion stops at some depth in the target, which is called the penetration depth. The collisions between these atoms are governed by the interaction potential between them. Nuclear

stopping is elastic and the classical interaction between atoms drives from the attractive chemical binding between them and the repulsive Coulomb forces between nuclei. The energy T transferred from a projectile with mass M_1 and kinetic energy E_0 to a stationary atom with mass M_2 in a collision can be solved by using the center of mass (CM) frame and calculating the scattering interaction [26, 27], which gives

$$T = 4\frac{M_1 M_2}{(M_1 + M_2)^2} E_0 \cos^2\theta, \tag{3.3}$$

where θ is the scattering angle. To calculate the magnitude of the nuclear stopping, the energy transfer cross section $\sigma(E_0, T)$ can be used, where σ gives the probability of a collision with an energy transfer T. The energy transfer cross section can be constructed by the full trajectories of colliding particles, which are determined from interaction potential between particles. Therefore, the path of colliding particles at all time must be such that the sum of the potential and kinetic energies equals the kinetic energy of trajectories. The nuclear stopping power is then given by

$$S_n(E_0) = -\frac{dE_0}{dx}\frac{1}{N} = \int_{T_{min}}^{T_{max}} T\sigma(E_0, T)dT, \tag{3.4}$$

where N is the atomic density.

3.4.2 Electronic stopping

Electronic stopping S_e is caused by interaction between atomic projectiles and bound electrons. The slowing down mechanism is due to the inelastic collision between electrons in the target and recoils going through it [28]. The energy lost by recoils is spent through the electron cloud into thermal vibrations of the target atoms. This phenomenon is well known for very high energy recoils, where the kinetic energy of recoil is on the order of MeV, while nuclear stopping is dominant at lower recoil energies, especially for heavier projectiles. This phenomena is described well theoretically by the Bethe formula [29] for electronic stopping at high energies. For low kinetic energy range where the ion carries atomic electrons, the electronic stopping of charged ions is described by modern Bethe-Bloch theory [30].

For low energy recoils that are not completely ionized, it is more complicated to calculate S_e theoretically [31]. By using Brandt-Kitagawa theory [32], the charge state of the ion is taken into account. Therefore, S_e is best to be determined semi-empirically by correlating both experimental and theoretical values by using e.g. the SRIM/TRIM code tabulations [33, 34].

Figure 3.4 shows the ratio between nuclear and electronic stopping power. For light ions slowing down in heavy targets, the nuclear stopping power is weaker than the electronic at all energy ranges.

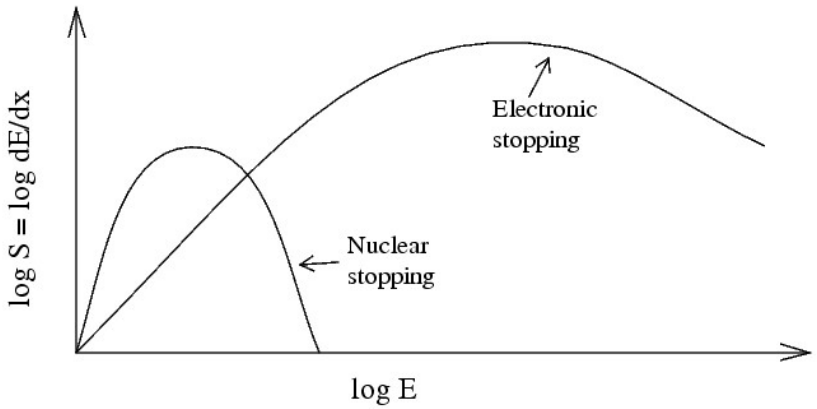

Figure 3.4: Ratio between nuclear and electronic stopping power. The maximum of the nuclear stopping curve is usually at energies between 10-100 keV, where as the electronic stopping power maximum is at MeV energies [35].

3.4.3 Implantation

An incoming particle from the edge plasma is either implanted in the target material or backscatered during an irradiation event. when an ion penetrates into a material and implants in a substrate. Different kind of phenomena may occur in the substrate, such as trapping, de-trapping, desorption, bubble formation and so on.

The main wall and the divertor of a fusion reactor is constantly irradiated by a large H-isotope flux coming from the edge plasma. Depending on the incoming ion energy and angle as well as substrate temperature of the material, H ions either penetrate deep in the bulk or are implanted near the surface of material. As the incoming ion energy increases, H ions penetrate deeper in the bulk and diffuse toward it as interstitials or get trapped in a defect which is created in the wall by the neutron irradiation and become immobile. In contrast, implanted H ions near the surface can recombine to form H_2 or hybrid molecules with the host surface atoms and release back to the surface as plasma impurities [36]. Furthermore, H ions mainly trap in defects and the implanted H may agglomerate to form larger defects such as voids, bubbles and blisters (see section 3.4.5) in solid materials [37]. Due to different characteristics of materials in defects and self-trapping, H bubble formation may happen in totally different depth in different materials.

Hydrogen isotope retention in plasma-facing materials due to implantation has been extensively studied for the JET device [38]. Different factors have been reported to affect H retention in PFMs such as the presence of trapping impurities in materials, incoming particle flux and energy and net damage in materials.

3.4.4 Reflection

Incoming ions from the plasma can be reflected back from the surface of the wall materials and be injected back to the plasma. For energetic ions, the incident particle transfers its charge and momentum and loses its energy to the target atom in a collision event and leaves the target

material after penetrating into a certain depth of the target material [39]. For lower incoming ion energy ranges, the reflection happens close to surface and the ion does not penetrate deep into the material. However, an ion is only reflected if the energy of the particle is above the binding energy of the surface. One of the important factors which effect the incoming particle reflection coefficient R_n is the mass of the target materials. For example, R_n for the 100 eV D ions is ≈ 0.4 in W, whereas the R_n for 100 eV D on Be was found to be 0.2 (Publication **II**). Moreover, increasing surface temperature lessens the amount of reflected D ions.

3.4.5 Erosion

Sputtering

The erosion of the PFCs surface is a highly critical issue [40]. *Sputtering* of materials is a process in which atoms or molecules are ejected from material's surface due to the bombardment by incoming particles from the edge plasma [41]. The sputtering yield Y of the removed surface atoms is determined by

$$Y = \frac{n_{sput}}{n_{impacts}}, \tag{3.5}$$

where n_{sput} represents the number of sputtered atoms and $n_{impacts}$ represents the total number of bombarded ions. Sputtering depends on a number of parameters such as mass ratio of incident particles to surface atoms, incoming particle energy and flux and angle of incident ion, as well as surface temperature [40]. Generally there are three main sputtering mechanisms: electronic sputtering, physical, and chemical sputtering.

Electronic sputtering occurs due to energetic electrons such as in a transition electron microscopy or because of very high-energy ion bombardment, where the electronic excitation can cause sputtering. However, the focus of this work is on physical and chemical sputtering.

Physical sputtering can happen in all materials independent of their structures. It results from the transfer of kinetic energy of the incoming particle to the target atoms on the surface layers. Bond breaking and therefore sputtering will happen if the energy received in the direction normal to the surface is sufficient to overcome the surface binding energy S_E [42]. Three regimes exist in this process: 1. If the energy is not enough to produce collision cascades, the sputtering occurs as a single knock-off event. 2. A linear cascade event can happen when a few cascades, but no sub-cascades are created. 3. When the incoming ion is heavy enough, the collisions occur very close to each other. In this case the binary collision approximation (BCA) [43] is not valid anymore (neither at low energies) and the collisional process should be understood as a complicated process of many-body interactions between thousands of atoms. This phenomenon also causes a heat spike [44].

Chemical sputtering occurs when the incoming particles form chemical compounds with the surface atoms by breaking and forming new bonds. Therefore, chemical sputtering is highly dependent on the surface materials and on the surface temperature, leading to processes such as thermal desorption and evaporation. To prevent such processes, a cooling system should be

designed in the reactor's first wall to control the wall's temperature to be always safely below a critical temperature. The erosion of hydrocarbons in fusion reactors is an examples of the chemical sputtering. On the other hand, molecules can form at the surface of certain materials by swift chemical sputtering (SCS). In the SCS process, an energetic particle penetrates between two substrate atoms, causing their bond to break, which release a surface atom together with any other atom bound to it. Both C and Be experience SCS effect under low energy H isotopes irradiation [45, 46]. The SCS played an important role during our studies for this thesis in the simulation of Be sputtering under low energy D irradiation (Publication **III** and **IV**).

Blistering

A large amount of PFMs can be eroded by the blistering phenomena under high irradiation fluxes and implantation fluences [47]. When irradiated ions are implanted in the target and agglomerate together, they displace the target atoms from their lattice sites, cluster together, and eventually form bubbles.This bubble formation near the surface in thick and loosely bound co-deposits can be observed as blisters [48]. Due to high ion gas pressure which is applied in the same direction as irradiated ion, the blister is ruptured and the above layers fly off. In publication **II**, H-induced blister formation is reported at the depth of projected range. In fusion devices, this effect results in emission of wall materials which have a serious effects on the power loss of the plasma.

Chapter 4

Methods

Several experimental devices exist to study the behavior of materials under irradiation in fusion reactors, such as small fusion reactors and linear plasma devices. However, the experimental studies cannot always explain the exact mechanisms participating in the PWIs. Therefore modelling can be used to complete the study of PWIs, building a bridge between theory and experiments. Computer modelling has a very significant role in fusion research besides the experimental studies in an extremely controlled condition. In this chapter, the basic principles of classical molecular dynamics (MD), binary collision approximation (BCA) and kinetic monte carlo (KMC) are explained and briefly characterized. Special attention is paid to the MD interaction models, which were used in all the publications of this thesis.

4.1 Classical Molecular Dynamics

Molecular dynamics (MD) is a simulation method based on solving classical equations of motion for each atom in the system. Currently, MD can be used on systems with millions of atoms. The popularity and applications of MD have been increased with increasing computational power since its first use in the 1950's [49]. In MD simulations the computational time is usually a linear function of the number of atoms in the system.

4.1.1 The MD algorithm

MD solves Newton's equation of motion for atoms. It can be based on quantum-mechanical interactions, but the simulations used in this thesis are based on the classical MD method, the Born–Oppenheimer approximation [50]. This approximation states that the dynamics of electrons is so fast that they reach the equilibrium well before the nuclei do. Thus, the two subsystems may be treated separately. The forces interacting between atoms are given by a so called *interatomic potential*. The effect of the electrons is approximated as a single potential energy surface and electronic effects like the formation of atomic bonds, are included in the interatomic potential which is used.

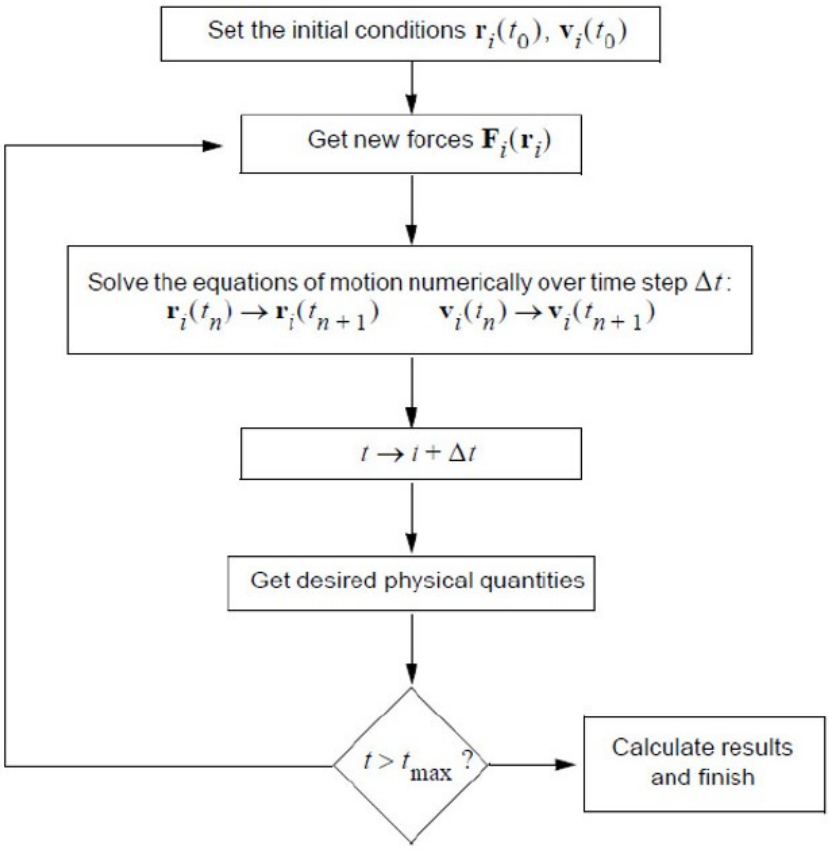

Figure 4.1: Flowchart of the basic MD algorithm

Figure 4.1 describes the algorithm for an atomistic MD simulation. The algorithm starts with setting initial positions $\mathbf{r}_i$ and velocities $\mathbf{v}_i$ of the atoms i = 1 ... N. Then, Newton's equations of motion for this system are solved numerically for the given atomic configuration $(\mathbf{r}_i(t), \mathbf{v}_i(t))$,

$$\mathbf{F}_i(\mathbf{r}_i, t) = m_i \ddot{\mathbf{r}}_i = m_i \mathbf{a}_i(t) = -\nabla_{r_i} V(\mathbf{r}_i), \tag{4.1}$$

where m_i, $\mathbf{r}_i(t)$, $\mathbf{a}_i(t)$ and $\mathbf{F}_i(\mathbf{r}_i, t)$ are the mass, position, acceleration and force acting on the atom i at a time t, respectively, determined by the interatomic potential $V(\mathbf{r}_i)$. The accelerations for the atoms can be calculated from this equation.

This equation is solved at each time step to calculate the new atomic configurations. In all simulations, the timestep must be much smaller than the fastest vibrational frequency in the system. When the timestep gets smaller, the number of steps needed to reach the final time increases and the modeling becomes computationally less efficient. In most MD simulations the timestep is a few femtoseconds (fs).

The integrations of Eq. 4.1 are done numerically at each time step, using an accurate and efficient integrator algorithm. For example, the Gear 5 predictor-corrector algorithm [50] is employed in the MD code PARCAS [51] used in this thesis to achieve numerically stable solutions. In a predictor-corrector method, first a prediction for the result is made and then this result is corrected in a second step. The corrector step can use different methods to refine the result by using the old data. After computing the accelerations, the new positions for the atoms can be calculated. With the given timestep (Δt) the new predicted position can be calculated as

$$\mathbf{r}_{i+1} = \mathbf{r}_i + \mathbf{v}_i\Delta t + \frac{1}{2}\mathbf{a}_i\Delta t^2 + \frac{1}{6}\mathbf{b}_i\Delta t^3 + \frac{1}{24}\mathbf{c}_i\Delta t^4 + \frac{1}{120}\mathbf{d}_i\Delta t^5, \tag{4.2}$$

where $\mathbf{r}_i$ and $\mathbf{v}_i$ are the old position and velocity, respectively, and $\mathbf{a}_i$ is the calculated acceleration where $\mathbf{b}_i$, $\mathbf{c}_i$ and $\mathbf{d}_i$ are the 3^{rd} to 5^{th} time derivative of $\mathbf{r}_i$, respectively. The new velocity of the atom is determined by

$$\mathbf{v}_{i+1} = \mathbf{v}_i + \mathbf{a}_i\Delta t, \tag{4.3}$$

After calculation of new positions and velocities, the list of nearby atoms for each atom in the system must be updated, usually done every $\sim$10 simulation steps.

Moreover, periodic boundary conditions (pbc) are used to simulate bulk materials and infinitely long wires without having to simulate too many atoms. The substrate cells were created by thermalizing the desired structure representing the bulk structure of the material. In this configuration, the pbc are applied in three (x, y and z) directions in this relaxation. Next, for opening the surface of the cell and to prepare it for irradiation at z direction, the pbc are applied only in the x and y directions.

Most often the temperature of the system must be controlled throughout the simulation. There can be a variation of the initial temperature of system; a cooling of the system to release the excess of energy introduced by recoils, heating up to relax the system or the system is kept at constant temperature during the whole simulation. In this method, the initial temperature is achieved by using Boltzmann distributed temperatures for all atoms, so all atoms will not have exactly the same kinetic energy. In PARCAS, the temperature is controlled by using the Berendsen thermostat method [52]. Here the system temperature T is controlled by coupling it to an external heat bath at a temperature T_0. Thus, the system's temperature will relax exponentially to the desired T_0 with a time constant τ,

$$\frac{dT}{dt} = \frac{T_0 - T(t)}{\tau}, \tag{4.4}$$

where $T(t)$ is the temperature of the system at time t. In MD, this is implemented as a friction term in the equation of motion (Eq. 4.1), since the temperature of the system is defined by the velocities of the atoms in it,

$$m_i\mathbf{a}_i(t) = \mathbf{F}_i(\mathbf{r}_i, t) - m_i\gamma(\frac{T_0}{T} - 1)v_i, \tag{4.5}$$

where $\tau_t = (2\gamma)^{-1}$ is the time constant. Therefore, the system temperature T is coupled to the desired T_0 by scaling the momentum of the particles by a damping constant λ, where

$$\lambda = \sqrt{1 + \frac{\Delta t}{\tau_t}(\frac{T_0}{T} - 1)}, \tag{4.6}$$

In a similar way to the temperature control, the pressure control can be achieved by scaling the positions instead of the velocities of atoms. Depending on the simulation setup, it is desired to maintain the system at constant pressure and let the volume V of the simulation box fluctuate. To achieve this, the Berendsen pressure control [52] scales the atom coordinates and the simulation cell dimensions by multiplying them by,

$$\mu = \sqrt[3]{1 - \frac{\Delta t}{\tau_P}(P - P_0)}, \tag{4.7}$$

where P_0 is the average pressure of the system, P is the desired pressure and τ_P is the time constant that determines the pressure scaling rate, as in the temperature control.

During our simulations, the temperature was controlled at all times; first, thermalizing the substrates while creating them, and later during the irradiation events in order to to remove the excess energy introduced by the projectile. In contrast, the pressure control was only applied when creating the substrates, while no pressure control was applied in the system during irradiation events.

In PARCAS some of the electronic effects which has already been explained is included in the algorithm. For instance, electronic stopping is modeled by scaling the recoil velocity at each time step Δt by

$$\Delta\mu = \Delta t \frac{S_e}{m}, \tag{4.8}$$

where S_e is the electronic stopping and m is the recoil mass. During this thesis, S_e is applied to all atoms with a kinetic energy larger than 1.0 eV which are not eroded.

4.1.2 Interatomic Potentials

The result and accuracy of MD simulations depends on the forces acting between the atoms. Therefore, the most critical part of the MD simulation algorithm is the calculation of these forces from the interatomic potential $V(\mathbf{r}_i)$ (see Eq. 4.1). So, developing desired potential models that can describe the interaction between atoms in a solid well, is vital. These potentials depend on different parameters. In general, they consist of attractive and repulsive terms, to account for the attractive and repulsive interactions between electrons and nuclei, due to the different charge signs, at different interatomic distances. Although these potentials are classical, their parametrization and formalism is usually derived from quantum mechanical principles.

Brenner-Tersoff-like analytical bond-order potentials

An analytical bond-order potential (ABOP) is able to describe variations of the local chemical environment, such as bond-breaking. Examples of ABOPs include the Tersoff potential [53], the Brenner potential [54], the Finnis-Sinclair potentials [55] and the second-moment tight-binding potentials [56]. The ABOPs were initially developed by Tersoff to describe covalent solids, but it was shown by Brenner and Albe [57] to be extendable to metals.

For a Brenner-Tersoff like potential, the bonding strength between two atoms depends on the number of neighbors around, where more neighbors results in a weaker bond. Moreover, the reactivity of ABOPs can describe breaking and formation of bonds. This is important in any system with chemical reactions. Although, this can result in computationally expensive simulations. The total energy in a Brenner-Tersoff like ABOP is expressed as a sum over individual bond energies:

$$E = \sum_{i>j} f_{ij}(r_{ij}) \Big[V_{ij}^R(r_{ij}) - \underbrace{\frac{B_{ij} + B_{ji}}{2}}_{\overline{B_{ij}}} V_{ij}^A(r_{ij}) \Big], \tag{4.9}$$

where r_{ij} is the distance between the atoms i and j, and $V_{ij}^R(r_{ij})$ and $V_{ij}^A(r_{ij})$ are the repulsive and attractive terms of the potential, respectively.
These are pair potentials given by Morse-like terms,

$$V^R(r) = \tfrac{D_0}{S-1} exp\Big(-\beta\sqrt{2S}(r - r_0)\Big), \tag{4.10}$$

$$V^A(r) = \tfrac{SD_0}{S-1} exp\Big(-\beta\sqrt{2/S}(r - r_0)\Big), \tag{4.11}$$

where D_0 is the dimer binding energy, r_0 is the equilibrium bond distance and S is an adjustable parameter. The parameter β can be determined by the ground state oscillation frequency of the dimer.

The cut-off function $f_{ij}(r_{ij})$, defines the interaction range, which is usually restricted to the nearest neighbor and given by,

$$f(r) = \begin{cases} 1, & r \leq R - D, \quad (4.12a) \\ \frac{1}{2} - \frac{1}{2}\sin[\pi(r-R)/(2D)], & |R - r| \leq D, \quad (4.12b) \\ 0, & r \geq R + D, \quad (4.12c) \end{cases}$$

where R and D are parameters determining the cutoff range and interval, respectively.

The bond-order parameter $\overline{B_{ij}}$ in Eq. 4.9, introduces the three-body interactions and angular dependence to the potential,

$$B_{ij} = (1 + \chi_{ij})^{-\frac{1}{2}}, \tag{4.13}$$

where

$$\chi_{ij} = \sum_{k(\neq i,j)} f_{ik}(r_{ik}) g_{ik}(\theta_{ijk}) \exp[2\mu_{ik}(r_{ij} - r_{ik})], \tag{4.14}$$

Here, μ_{ik} is a fitting parameter and again the cutoff function is included, while the indices monitor the type dependence of the parameters, which is important for the description of compounds. The angular function g_{ik} is of the form:

$$g(\theta_{ijk}) = \gamma\left(1 + \frac{c^2}{d^2} - \frac{c^2}{[d^2 + (h + \cos\theta_{ijk})^2]}\right), \tag{4.15}$$

where γ, c, d and h are adjustable parameters. In the case of c = 0, where the angular function becomes a constant, the total potential resembles an embedded atom method (EAM) potential, used to model the pure metal interaction. EAM potential is explained in details during this section.

The ABOPs are suitable for studies regarding plasma–wall interactions in fusion reactors, since they are able to model non-equilibrium phenomena such as particle irradiation, sputtering and the formation of mixed materials. They can describe pure metals such as Be and W well. Therefore, it is an appropriate tool to model the full W-C-Be-H system. This Brenner-Tersoff like potential was used for publications **II-IV** and is explained in Refs. [58, 59]. In publication **I** to model the ternary Fe-C-D systems, the Brenner-Tersoff like potential which is suitable for describing both metallic and covalent bonds, was used [60]. The potential calculation was modified in such a way that C-C, C-D and D-D parameters are given by Brenner's second parametrization [54], while for bonds involving Fe atoms, the Fe–C Tersoff potential [61] was used.

The embedded atom method

The embedded atom method (EAM) is a model that is suitable for metals, where atoms are treated to be planted in a sea of electrons [62]. The energy in EAM is expressed as a function of the electron density,

$$E = \sum_i F_i(\rho_i), \tag{4.16}$$

where F_i is the embedding energy, and ρ_i is the electron density of an impurity at the atom site *i*. To determine the term F_i, The Finnis-Sinclair solution [55] can be derived from second-momentum approximation of the tight-binding theory in solids [63],

$$F_i(\rho_i) = -A\sqrt{\rho_i}, \tag{4.17}$$

where A is a fitting parameter.
Practically, a correction term to represent the pair potential must be added to the total energy for the short-range repulsive interaction. The total energy of a system is given by,

$$E = \sum_i F_i\left(\sum_{j\neq i} \rho_j(r_{ij})\right) + \frac{1}{2}\sum_{i,j\neq i} V_{ij}(r_{ij}), \tag{4.18}$$

The short-distance interaction

In order to get the equilibrium properties of interactions in a system, the potentials are fitted. Although, the repulsive interaction between the nuclei at short distances can be underestimated by this description. This short-distance regime is also important for high-energy interactions. A good choice for the repulsive potential in this case is the Ziegler-Biersack-Littmark [31] function which is given by

$$\Phi(x) = 0.1818e^{-3.2x} + 0.5099e^{-0.9423x} + 0.2802e^{0.4029x} + 0.02817e^{-0.2016x}, \tag{4.19}$$

with $x = \frac{r}{a}$ and

$$a = \frac{0.8854a_0}{{Z_s}^{0.23} + {Z_p}^{0.23}}, \tag{4.20}$$

where a_0 is Bohr radius, and Z_p and Z_s are projectile and substrate atomic numbers, respectively.

4.2 Binary Collision Approximation

One of the widely accepted techniques employed for investigating sputtering and for studying ion irradiation induced damage at surfaces, which is important at higher energies, is the Binary Collision Approximation (BCA) [43] which is illustrated in figure 4.2. In BCA it is assumed that the collisions between atoms can be approximated by elastic binary collisions. In this technique, a single collision between the incoming ion and a target atom is treated by solving the classical scattering integral between two colliding particles [64]. Solution of the integral results in both scattering angle of the incoming ion and its energy loss to the target atom. The scattering angle between the ion and the target atom is calculated as

$$\theta = \pi - 2\int_0^{\frac{1}{\rho}} (\frac{1}{p^2}[1 - \frac{V(u)}{E_1}\frac{(m_1 + m_2)}{m_2}] - u^2)^{\frac{-1}{2}} du, \tag{4.21}$$

where $u = \frac{1}{r}$ and r is the interatomic distance. $V(u)$ is the interatomic repulsive pair potential and ρ is the nearest possible distance for *r*. E_1 and m_1 are the impacting energy and mass of the projectile respectively, and m_2 is the mass of the target atom.

The interatomic potential is usually a screened Coulomb potential of the form

$$V(r) = \frac{1}{4\pi\epsilon_0}\frac{Z_1 Z_2}{r}\Phi(\frac{r}{a}), \tag{4.22}$$

where Z_1 and Z_2 are the magnitudes of the charges, the scalar *r* is the distance between the charges and ϵ_0 is the electric constant. The ZBL screening function can be used for $\phi(\frac{r}{a})$, where $\frac{r}{a}$ is screening length [33].

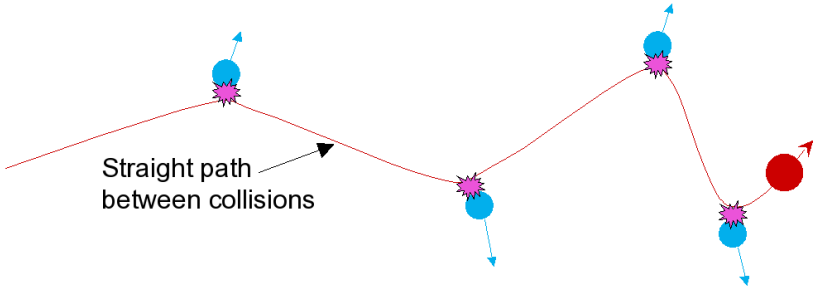

Figure 4.2: Schematic illustration of binary collision between atoms. Image extracted from *wikipedia*

The energy loss of an incoming ion to target electrons can be handled separately as an inelastic energy loss. This energy loss process reduces the energy of the incoming ion, but does not change the direction of that. A target surface layer atom is considered to be sputtered if its energy normal to the surface is larger than the surface binding energy.

The advantage of BCA is its speed, which is 4-5 orders of magnitude faster than MD. This approximation is reasonable for high-energy recoils where the surface binding energy is small compared to the recoil energy of the atoms. Therefore BCA is based on some assumptions and limitations. This approximation can arise at low ion energies, in very dense materials, or when chemical effects play a role in materials.

There are many computer simulation programs based on BCA dealing with crystalline and amorphous targets. Static Monte-Carlo program which is known as transport of ions in matter TRIM [65] is one of the programs dealing with amorphous targets. The reciprocal dynamic version of that is TRIDYN [66] which can describe collision effects in solids [67]. SDTrimSP (where S stands for static and D for dynamic) is the combination of the two mentioned programs with all possible output facilities used before, such as sputtering, backscattering and transmission. The basic physics in the new program SDTrimSP [68] is the same as the former versions. It assumes an amorphous target structure at zero temperature and infinite side size and treats the bombardment of incident ions on different target structures. in publication **I** the BCA results were mainly used as a comparison to MD simulations.

4.3 Kinetic Monte Carlo

The Monte Carlo (MC) techniques, named after a casino in Monaco, are generally the numerical methods to solve problems by random sampling [69]. The MC algorithm is relied on randomly sampling the different processes that can happen in a system, according to their probabilities, i.e., rates [70]. MC method has an extremely wide range of application, from the formation of clusters of galaxies [71] to the particle diffusion in a solid [72] and the impurity migration in the fusion edge plasma [73].

4.3.1 Basic approach

One approach for simulation of the time evolution of a system by the MC method, is called Kinetic Monte Carlo (KMC). The main idea behind KMC is to use transition rates between the states, formulated with the time increment.

The KMC algorithm starts by taking all the possible transitions of the system R_i and their transition rates r_i should be listed and therefore the cumulative function is calculated accordingly,

$$R_i = \sum_{k=1}^{i} r_k, i = 1...N. \tag{4.23}$$

In the next step, by generating a uniform random number, $\mu \in [0, 1]$, an event *i* is found for which

$$R_{i-1} < \mu R_N < R_i \tag{4.24}$$

The chosen event *i* is carried out within the code and further consequences that event *i* might lead to, are investigated. After that, the time *t* is updated, $t \rightarrow t + \Delta t$. Δt is calculated by generating a new uniform random number $\nu \in (0, 1]$,

$$\Delta t = -\frac{ln(\nu)}{R_N}, \tag{4.25}$$

Finally, all the wanted properties of the system are calculated and the output is reported. Before choosing a new event, all the rates and cumulative function R_i are updated. The mentioned steps and algorithms are repeated until the desired number of events and time is reached.

KMC algorithm deals only with rates, therefore just by knowing the set of rates in a system, the system can be easily simulated without considering its thermodynamics. The big advantage of KMC is that, as the cumulative function R_i is recalculated every step depending on the objects present in the system, the time scale Δt of the steps will follow the system evolution automatically. The system can switch to shorter or longer time scale according to the remaining objects in the system. For instance, if slow-moving objects are left in the system after fast-moving objects have reacted and gone, the time scale will get automatically longer for the remaining objects. Because of this feature of KMC, in many simulations, the initial time scale is of order of *fs*, whereas the final one can be in the order of minutes or even years.

On the other hand, the main drawback of KMC is that all possible rates r_i and possible reactions need to be known in advance to develop a KMC algorithm. However, most of the rates can be obtained from experimental data or calculated from other atomistic simulations methods such as BCA or MD, or, quantum mechanical calculations i.e. density functional theory (DFT) [74]. Another disadvantage of KMC might be from computational efficiency point of view due to creating all the lists and recalculating r_i in each time step, especially when there are a large number of possible transitions in the system.

4.3.2 Object Kinetic Monte Carlo

When the modeled processes in KMC are enforced for objects such as impurities, dislocations or defects, the method is known as Object Kinetic Monte Carlo (OKMC). OKMC is one of the best and preferred techniques to study defect evolution in solid materials [75, 76]. The model assumes that there are several different states in a system and the transitions between these states are known and independent of time. These transitions are the input parameters of the algorithm, and the dynamic evolution of the system out of equilibrium is followed by OKMC [77–79]. Since OKMC only takes into account defects (self-interstitial atoms, vacancies, impurities and their clusters) but not the lattice atoms themselves, simulation boxes of the order of few micrometers and large time scales of the order of hours (even days) can be simulated. Different OKMC algorithms exist, depending on the modelled processes, objects, probabilities and interactions. One of such models designed to study long term evolution of damage in irradiated solids, for instance in fusion reactor materials, is called MMonCa [80].

In MMonCa, the objects are defined as defects that introduce undesired effects on material applications. MMonCa needs two sorts of input data: (i) an activation energy and a prefactor for each transition that might happen, such as migration or dissociation of defects and (ii) the initial positions of the defects present at the beginning of the simulation.

Migration and dissociation probabilities are calculated with an Arrhenius law

$$\nu = \nu_0 . e^{-}(\frac{E_{event}}{k_B T}), \tag{4.26}$$

where ν_0 is the prefactor, E is the corresponding energy barrier, k_B is the Boltzmann constant, and T is the temperature of the system.

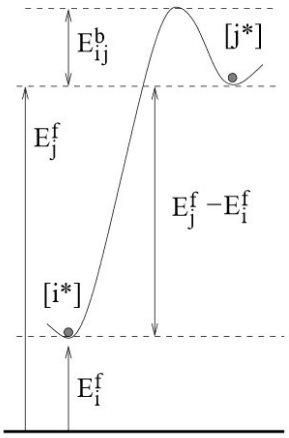

Figure 4.3: Energy diagram for the MMonCa simulator. The picture shows the barrier and formation energies at two *i* and *j* states. Image reproduced from Ref. [80].

The physical meaning of these energy barriers is illustrated in Fig. 4.3. In this simulator, defect evolution in solids is followed by three modules:
1) objects or defects and all their possible transition rates and interactions
2) computing time evolution by a rate manager
3) creating spatial transitions and defect interactions by a space manager

Previously, the MMonCa has been successfully applied to study low energy helium irradiation on tungsten for a wide range of temperatures, to determine tungsten fuzz growth [81]. In this thesis, in publication **IV**, we used MMonCa to investigate the effect of surface temperature on the D depth profile in Be. The barrier for migration and formation of all mobile objects are obtained from literature, mostly with DFT calculations. In our OKMC simulations, many aspects of D migrations and defect diffusion in ITER first-wall relevant conditions, were examined.

Chapter 5

Sputtering of Iron-based alloys for DEMO applications

Various steels are being examined as PFMs for the main wall of DEMO. Since steels are alloys of Fe and C, it is highly critical to quantify the erosion of both elements when being exposed to plasma particles. In publication **I** the effect of D irradiation on ferrite, Fe with 1% C impurity and the cementite surface erosion and morphology changes was investigated. For that reason, cumulative bombardment of D ions on above mentioned surfaces was carried out by MD and dynamic BCA simulations varying impact energies and substrate temperatures. The exact details of the simulation set up can be found in **I**. It should be noted that, during the simulations, an atom or cluster of atoms was considered sputtered and taken out of the system if they were no longer bonded to the surface of the sample.

In general, the sputtering yield of both Fe and C were found to increase with impact energy. The effect of substrate temperature for the surfaces studied in **I** was found to be negligible.

Figure 5.1 illustrates Fe sputtering yields in pure Fe and Fe-1%C from MD and compared to the experimental outcome by Hintz [82] and Bohdansky [83], varying impact energies. The figure shows excellent agreement between simulation and experiments.

We found that the number of reflected D atoms varied greatly with the impact energy and the trapped D in Fe-based C-containing alloys forms D_2 molecules. Moreover, in the Fe-1%C and Fe_3C simulation cells, C atoms where found to trap more D ions, which resulted in lower D reflection in comparison with the pure Fe simulation cell at 500K. Figure 5.2 shows the fraction of D ions not implanted in the Pure Fe and Fe-1%C, simulation cells. For impact energies higher than 100eV, a large fraction of irradiated D went through the simulation cell, and ions were retained in the bulk.

Further, after a few hundred irradiations the Fe_3C lattice started to lose its crystallinity in D rich areas, while the percentage of amorphous volume increases with increasing D influence. Moreover, the surface erosion is not homogeneous, which leads to surface roughening. These

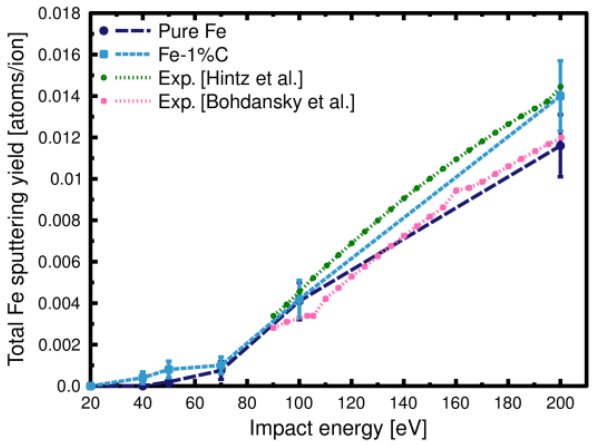

Figure 5.1: A comparison of Fe sputtering yields in ferrite and Fe-1%C between MD simulation and experiments at different impact energy. During the simulations the substrate temperature was set to 500K. From publication I.

findings correlate well with previous MD study of cumulative irradiation of Fe_3C with Fe recoils [84]. As shown in Fig. 5.3, at energies higher than 70eV, D ions were implanted deeper in the cell, forming D_2 bubbles. For even higher energies, we predicted to see the same event that happened in WC [85], where with increasing D influence, the D_2 accumulation could result in a blistering-like effect. However the higher C percentage in the system simplifies the formation of D_2 molecules in the system.

The key result of **I** is the preferential C sputtering during the bombardment in Fe_3C specially in the 40-150eV energy range, where the surface was enriched with Fe. Figure 5.4 illustrates that C sputtering dominates over Fe sputtering in cementite. However, the sputtered C atoms were mainly in atomic form and the number of each sputtered species after 3000 D impacts on Fe_3C at different energies are shown in a table in publication **I**. Analysing the sputtering mechanism of Fe and C showed that it is dominantly of physical origin at impact energies higher than 100eV, while at lower impact energies, the sputtering mechanism was of both physical and chemical origin.

On the whole, the results in publication **I** show that if steels are used at PFMs, the existence of C in them will cause chemical sputtering of C-containing molecules. Carbon transport and inventory calculations are required to assess whether this will lead to re-deposition of significant amounts of C during prolonged operation, and specially C-bound tritium, elsewhere in the reactor.

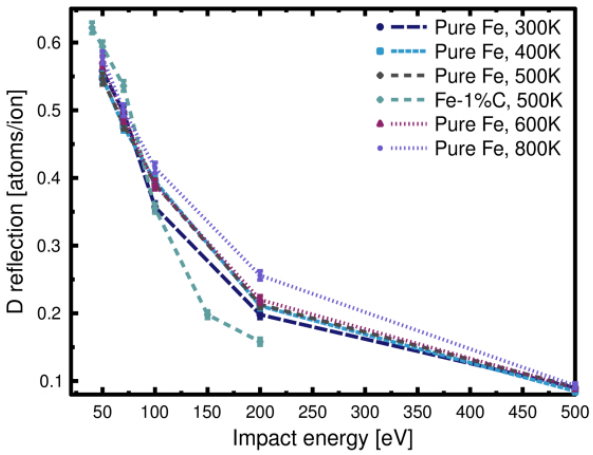

Figure 5.2: The D reflection of pure Fe at different temperatures and Fe-1%C at 500K as a function of energy, obtained after 5000 cumulative D impacts. From publication I.

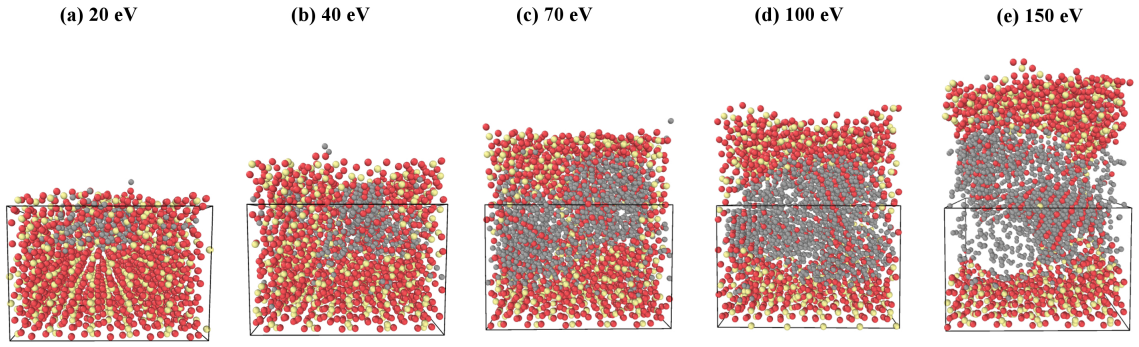

Figure 5.3: Structure of Fe_3C after 3000 D impacts with different impact energies, for a substrate temperature of 500K. Red, yellow and grey spheres represent Fe, C and D atoms, respectively. From publication I.

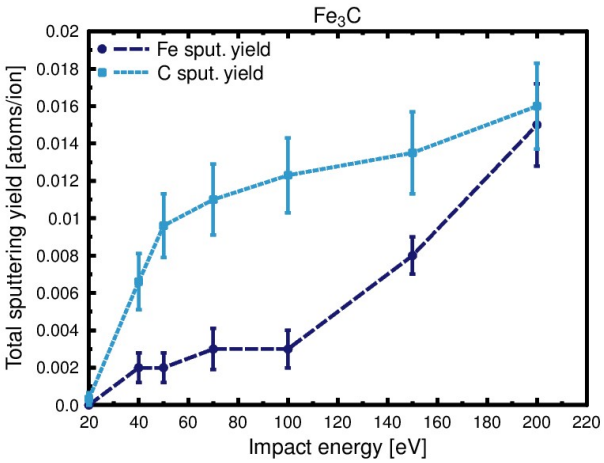

Figure 5.4: Total Fe and C sputtering yield as a function of impact energy of Fe_3C erosion by 3000 cumulative D irradiation. From publication I.

Chapter 6

Co-bombardment of W and Be

In fusion reactors, to lessen the particle and local power load onto wall materials, impurity seeding to the plasma is needed as a method to remove excessive heat flux [86]. For instance in ITER, this can be achieved by puffing noble gas impurities in vacuum vessel manually [87]. These plasma impurities interact with PFCs and can cause sputtering and modification of wall components, as well as affecting both D release and retention in W and Be [88–90]. The interaction between plasma impurities such as D, Ne and Ar with W and Be using MD were studied in publication **II** by irradiation of a mixture of *x*%Ar or Ne with *(100-x)*%D (*x*=0, 5, 10 and 20) on both W and Be surfaces varying the impact energy and surface temperature. Further details regarding to the simulation set up and method can be found in publication **II**.

6.1 Impurity effects on sputtering

Overall, W and Be erosion yields were higher in the presence of Ar and Ne plasma impurities in comparison with pure D irradiation. The magnitude of sputtering yields increased with increasing impact energy, while the effect of substrate temperature for the surfaces studied here was negligible.

W sputtering yields for pure D bombardments were zero for the cases studied here due to the high energy threshold of D sputtering As shown in Fig. 6.1, adding a few percentage of impurities to D ions can significantly affect W total sputtering yields, especially at higher energy of the impurity ions, which correlates well with previous experimental and modelling works [85, 88]. Moreover, the W molecular sputtering yield is really low, which is not enough for statistical analysis. However the existence of multiple such events is still an important result, where the analysis confirmed that W-W bond breaking phenomena combined with the high energies of the impurities means that the WD sputtering mechanism is likely physical rather than chemical sputtering. Furthermore, impurity bombardment on the Be surface results in higher Be sputtering yields, and increasing the energy of impurity ion increased single Be sputtering yields (figure 6.2). The effect of impurities on BeD_n molecular sputtering is less significant and most of the sputtered species were BeD molecules.

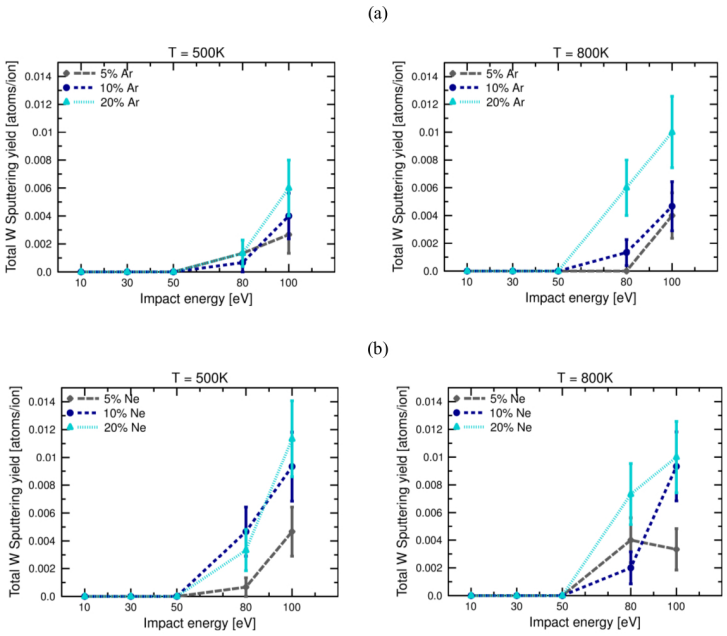

Figure 6.1: Total W sputtering yield as a function of impact energy at different surface temperature for 2000 (a) Ar-D and (b) Ne-D cumulative co-bombardment of W cells. From publication II.

A key result in **II** is that at impact energies lower than 50eV, adding noble gas impurities to D bombardments would not significantly affect the W and Be erosion yield. Furthermore, sputtering mechanism in low ion irradiation energy range is due to the swift chemical sputtering phenomenon, which means that Ar and Ne have very low probabilities to cause swift chemical sputtering. However, noble gases affect the total erosion of both W and Be targets at impact energies higher than 100 eV where physical sputtering is possible significantly. These findings correlate well with another MD modelling of H, He, Ne, Ar-bombardment of amorphous hydrocarbon structures, performed by P. Träskelin et. al. [91].

6.2 Materials modification

Deuterium reflection decreased with increasing ion energy in W and Be. This is simply due to increased kinetic energy which makes it easier to penetrate into the material instead of reflecting from the surface. During ion irradiation, the structure of both W and Be samples were damaged. At energies of 50 eV and below, amorphization of the W and Be surfaces were observed as the irradiation went on, i.e. the deuterium ions gathered at the surface, changing the structure from crystalline to non-crystalline due to the high concentration of deuterium.

For W simulations, at higher energies the surface itself remained almost completely intact during pure D bombardment, with damage happening deeper in the lattice. However, when noble gas impurities were introduced, at higher impact energies the surface experienced notable damage, it remained crystalline, but became much rougher. The amount of damage the surface received increased with both ion energy and impurity concentration. Figure 6.3 represents

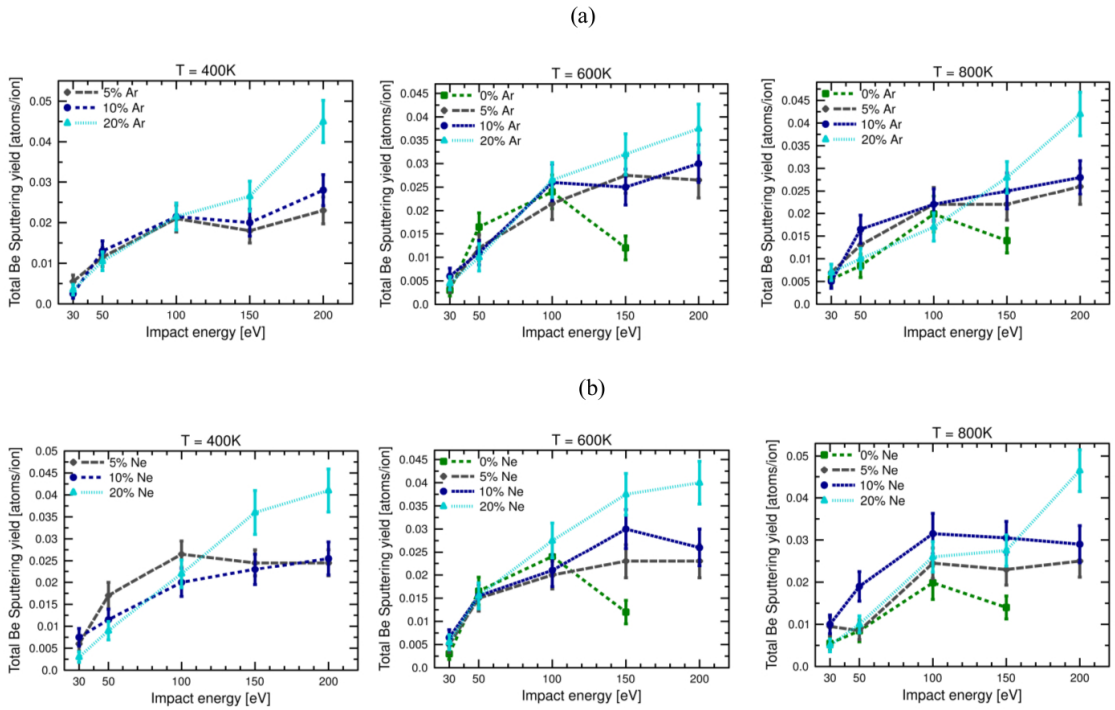

Figure 6.2: Total Be sputtering yield as a function of impact energy at different surface temperature for 2000 (a) Ar-D and (b) Ne-D cumulative co-bombardment of Be cells. From publication II.

W surface structures at 800K surface temperature due to 10% Ne-90%D co-bombardments at different impact energies. The structures reflect that D penetrates deeper into the surface with increasing impact energy, and is spread over a wider area. There is also more deuterium, which is consistent with D reflection decreasing with ion energy. Furthermore, concentration of noble gas impurities seems to have minimal effect on the D depth profile, except at higher energies where increased impurity concentration seems to cause slight depletion of D at the surface. Higher impurity concentrations lead to increasing D reflection yield, therefore the damage caused to the surface prevents deuterium atoms from building up near the surface.

Moreover, in Be, for energies lower than 100eV, a large fraction of D atoms and almost all the irradiated noble gases were reflected back from surfaces. For ion impact energies higher than 100eV, and therefore higher ion penetration depth, a large fraction of D atoms went through the sample and a small number of Ar and Ne atoms were also implanted, which results in observing amorphization deeper in the simulation cells. For this energy range, the D clustered in the center of the cell, mainly forming D_2 molecules. In a few cases, this D_2 accumulation results in separation of a D_2 layer, where the top layer of the cell was ruptured due to the high D_2 gas pressure, which can apply a force in z direction (blistering-like effect). The layers above flew off and the simulation was stopped in this case. However, surface rupture in W simulations was not observed here.

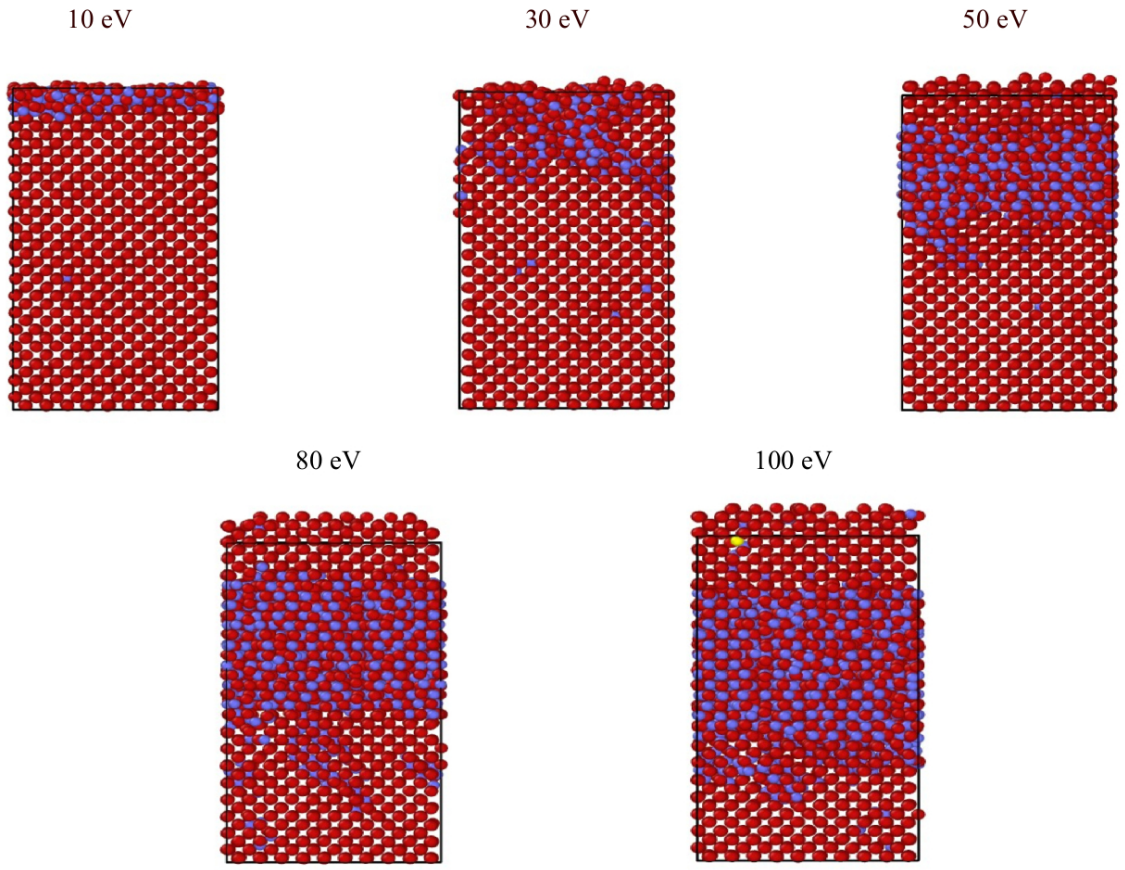

Figure 6.3: Surface morphology of W cells after 2000 10% Ne-90% D co-bombardments at different impact energies, for surface temperature of 800K. The W atoms are represented by red spheres, D atoms and Ne impurities are smaller light blue and yellow spheres, respectively. From publication II.

Chapter 7

Multi-scale modeling of Be erosion

As Be has been chosen for the main wall material of ITER, investigating the sputtering characteristics of the Be–D system is of vital importance. The purpose of publication **III** is to use MD techniques to gain insight into the effect of irradiation energy, particle flux and substrate temperatures on the Be erosion due to D irradiation under fusion relevant conditions. In this publication special attention is paid to release of BeD_n molecules. To estimate the stability of BeD_n molecules after sputtering, we also carried out quantum mechanical calculations of the molecules. Thermodynamic data for neutral BeD_n gas molecules were calculated using different approaches [92, 93].

In general, the Be surface morphology showed significant change at different surface temperatures under D irradiation with different energies. After only a few D impacts, the Be surface was damaged, the Be atoms had D atoms bound to them, and the deposition of D at the Be surface was able to cause surface amorphization at higher temperatures. Moreover, the erosion was not homogeneous, leading to surface roughening. Be surface morphology changes due to D irradiation is shown in figure 7.1. For the lowest substrate temperature (200K), the D atoms agglomerate in the center of the cell, mainly forming D_2 molecules and become rather immobile. The D concentration in this area increased with increasing D fluence. At 600K, the implanted D atoms migrated back and piled up around the surface, ending up mostly bound to Be atoms at the surface. At this temperature range, D could easily be desorbed when forming D_2 molecules, increasing the fraction of D released in molecular form. With increasing temperature, the atomic motion at the surface increased, resulting in a higher probability for atomic bonds to break, and thus D was able to desorb before even having time to form D_2 molecules. The highest temperature, 1440 K, is close to the Be melting point, leading to an increased Be sputtering due to the increased atomic vibrations that weaken the atomic bonds at high temperatures. At this temperature, around half of the cell was sputtered after 2000 D impacts.

We found that D implantation behaviour in Be at different surface temperatures highly affects the Be erosion behavior. As illustrated in figure 7.2, with increasing temperature, the Be sputtering yield increased at low impact energies (<150eV). At temperatures higher than 600K, there was a sharp increase in the yields because of surface deuteration and desorption at this temperature range. The molecular erosion showed a strong dependence on the topmost surface

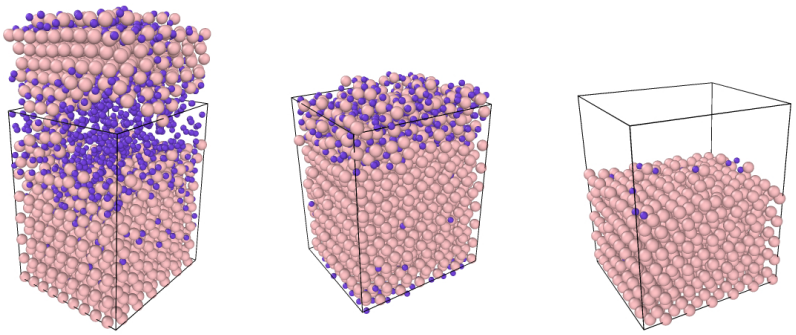

(a): T = 200 K (b): T = 600 K (c): T = 1440 K

Figure 7.1: Surface morphology of Be cells after 2000 impacts at different temperatures, for a particle flux of 2.02*10^{24} (cm^{-2} s^{-1}) (10 ps/impact). The D atoms are represented by small purple spheres and the Be atoms are the larger pink spheres. From publication III.

D concentration. At temperature lower than 500K, the D concentration at the topmost layer and consequent molecular erosion are low, and the main eroded molecular species was seen to be BeD. At higher temperatures (T $\approx$ 600 K), because of high D surface concentration the total sputtering yield of Be atoms increased rapidly and BeD_2 and BeD_3 molecules became the main eroded species, reducing the sputtered BeD:Be fraction. However, we studied the stability and dissociation of the larger molecules and found that the BeD_n molecules would dissociate as soon as they entered the edge plasma, mainly forming atomic Be and D_2 molecules, and not contributing significantly to the signals measuring the fraction of Be eroded as BeD. At even higher temperatures (T > 1000K), the Be was eroded in atomic form and as BeD molecules. These findings are presented in figure 7.3, and the simulated temperature dependence of the BeD release was in agreement with experiments performed at JET, which showed a linear drop in the BeD:Be ratio, i.e. Be sputtered as BeD, with increasing temperature in the range of 500–700K [94].

Our study in publication **III**, MD simulation of cumulative D impacts on Be surfaces, showed a complex outcome for molecular erosion. Due to very different D surface content at different surface temperatures, larger Be–D molecules were also emitted when the D concentration increased in the topmost layer. These results were non-physical for reactor-like conditions, caused by MD being limited to short time scales, and consequently high irradiation fluxes [95]. Therefore, the purpose for publication **IV** was to investigate erosion of equilibrium Be surfaces, in a KMC-MD multi-scale approach. The complex relationship between surface temperature and D surface content was appropriately calculated by a longer time-scale approach, the KMC technique. The KMC outcome provides initial substrate structures for MD closer to experimental condition, which allows gaining insight into the effect of surface temperature and irradiation energy on Be erosion.

In our OKMC simulations, many aspects of D migrations and defect diffusion in ITER first-wall relevant conditions, were examined. Eventually, the D distribution profiles at different

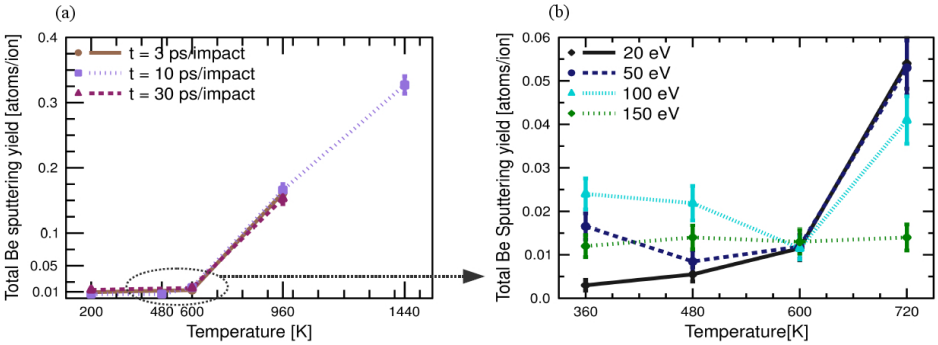

Figure 7.2: Left graph: total Be sputtering yield by D bombardment as a function of temperature for different particle flux and impact energies. Right graph focuses on JET-relevant surface temperatures. From publication III.

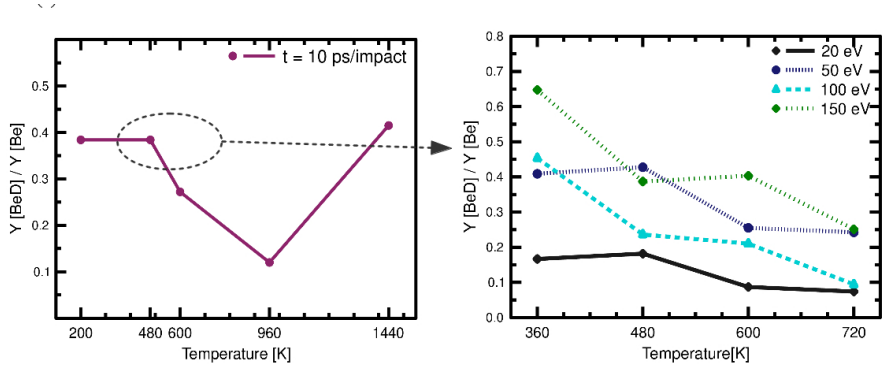

Figure 7.3: The fraction of Be eroded as BeD molecules for different simulation groups. From publication III.

temperatures were calculated from OKMC to set up accurate substrate structures in MD. Due to MD time scale limitations, diffusion evolution processes are not accessible by MD. Therefore, OKMC will assist MD to reproduce the simulation conditions closer to experimental conditions. Further details of all simulations set-up performed for this study can be found in publication **IV**. Figure 7.4 represents an OKMC cell after 1.2 seconds simulation time of D irradiation on Be at 700K surface temperature.

The equilibrium D distribution in Be for different vacancy concentrations for two different temperatures is illustrated in Fig. 7.5. The D atomic density can reach high values, especially near the surface. At 400K surface temperature, D atoms accumulate only in the first few surface layers, while in layers deeper than 6 nm, there is almost zero D concentration. With increasing temperature, D atoms distribute deeper and more evenly in the cell. Vacancies are more favourable defects to accommodate D atoms rather than interstitial sites in Be, therefore, higher vacancy concentration provides more traps for D atoms to accommodate and hence higher D concentrations. Therefore, a linear dependency of D distribution on vacancy concentration is observed. At higher temperatures, D atoms distribute more evenly and deeper in the cell, and therefore the D surface content decreases by increasing temperature.

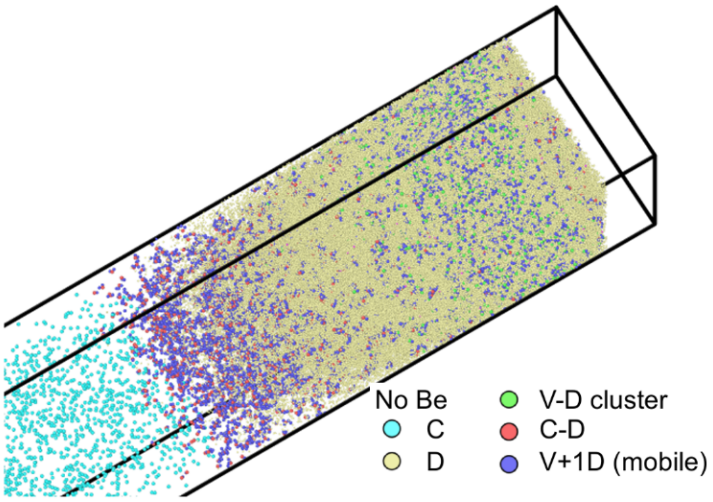

Figure 7.4: OKMC simulation cell after D irradiation at 700K surface temperature.

The key result of this OKMC simulation is that a strong temperature dependency of D concentration on the number of vacancies is observed during the simulations. At the early stages of our simulation, all vacancies were filled with up to 5 D atoms and all other incoming D atoms diffused in the cell as interstitial. D atoms tend to accommodate in a vacant site rather than becoming interstitial. As the simulation goes on, at lower temperatures, D atoms remain in vacancies and form immobile D_5V defects. At higher temperatures, D atoms are de-trapped from vacancies regularly because of their lower binding energy and diffuse fast toward bulk as an interstitial.

The final D profiles at 5% vacancy concentration (reasonable for mixed crystalline, and co- and re-deposited layers) to set up accurate substrate structures in MD at different temperatures are shown in figure 7.6.

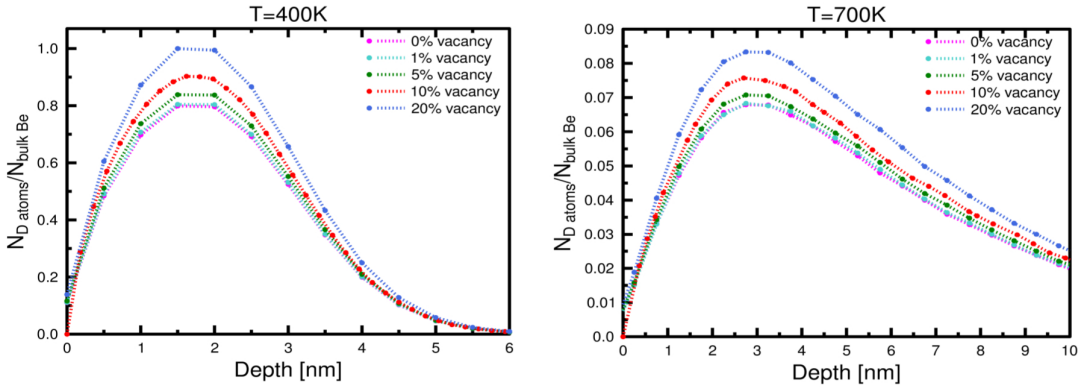

Figure 7.5: Equilibrium D distribution in Be for different vacancy concentration at 400 K (left) and 700 K (right). The number of D atoms in different layers is normalized to the number of Be atoms in bulk. From publication IV.

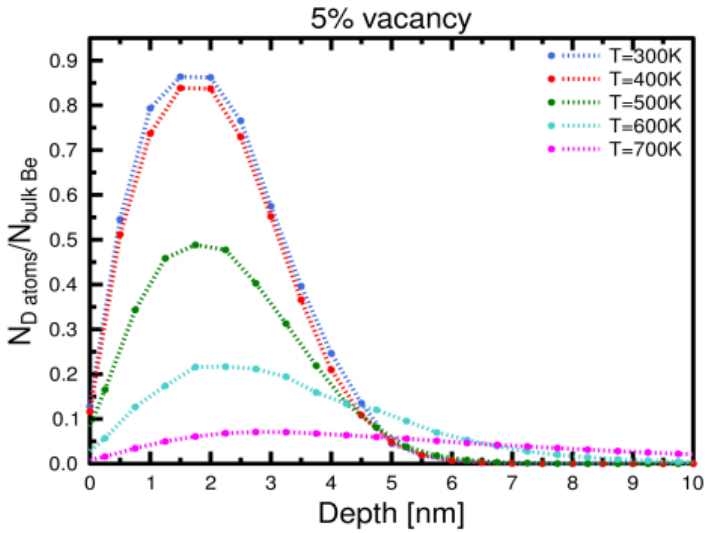

Figure 7.6: Equilibrium D distribution in Be at 5% vacancy concentration to set-up MD initial structures at different surface temperatures. From publication IV.

In the MD part of the work, there was no interest in further evolving the surfaces and hence the non-cumulative simulations were performed. With increasing surface temperature and hence reduced D surface concentration, the erosion yield of Be increased within the error bar, for ion energies greater than 10 eV. At lower surface temperatures where D concentrations are higher (there are more D neighbours to surface Be atoms), the probability of hitting a Be atom with incoming ion is lower than higher surface temperature, which leads to lower total Be erosion yield. With increasing impact energy, the total Be erosion yield increases with temperature, where it peaks at 100eV. For energies higher than 100eV, a reduction in total yield is observed, which is due to larger penetration depth of D ions at higher energies, which lowers the surface interactions.

A comparison of modelled and measured total Be sputtering yield at 300K surface temperature as a function of incident ion energy is presented in figure 7.7. The experimental yields were measured in PISCES-B facility, using a polycrystalline Be sample [96]. The difference between MD and experimental total Be yields is considerable, especially for impact energies higher than 60eV. However, the experimental yields still follow the same trend as in MD simulations.

The fraction of Be atoms that are sputtered as BeD molecules is illustrated in figure 7.8. Increasing both surface temperature and impact energy lead to a reduction of the BeD erosion yield. At higher temperatures and hence lower D concentration, there are less D atoms than what is initially bound to Be atoms, which lead to lower BeD erosion yield. Moreover, as the impact energy increases, single Be atoms are eroded via physical sputtering rather than swift chemical sputtering, lowering the BeD molecular fraction.

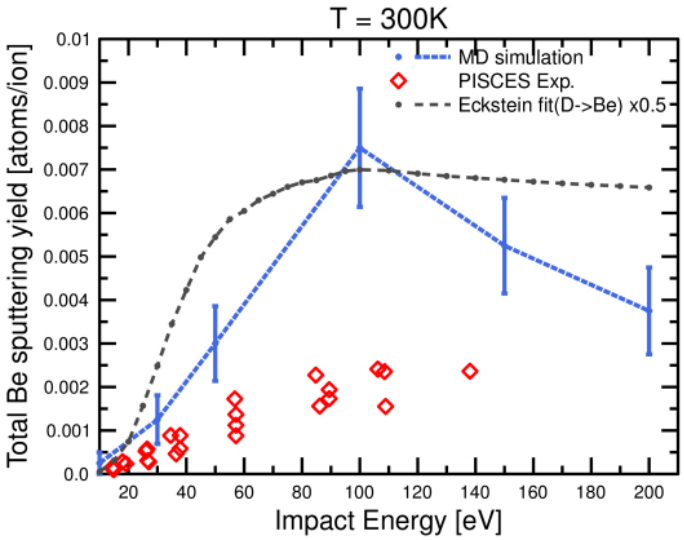

Figure 7.7: Comparison of modeled (by MD) and measured (by PISCES-B) total Be sputtering yield by D irradiation as a function of impact energies at 300 K surface temperature. The Eckstein fit is also plotted by a factor of 0.5. From publication IV.

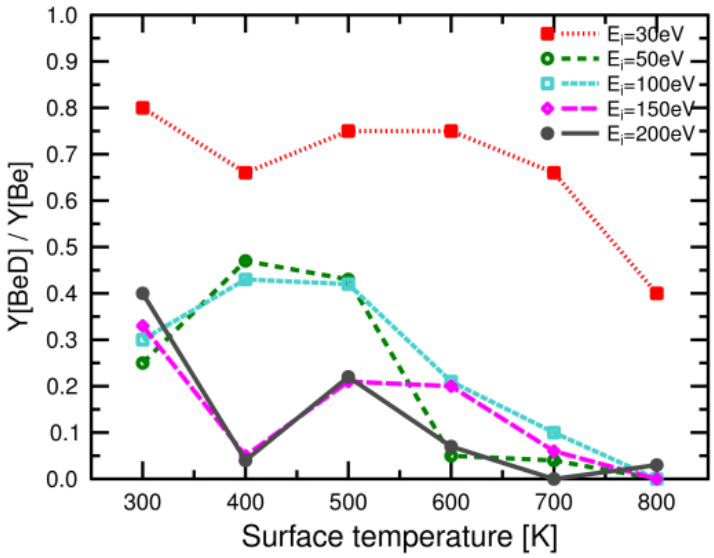

Figure 7.8: The fraction of Be eroded as BeD molecules as a function of surface temperatures for different impact energies. From publication IV.

MD simulations in both publications **III** and **IV** confirmed the reduction of sputtered BeD molecules with increasing temperature and ion energy, which showed a linear drop in BeD:Be ratio, as reported by experiments done at PISCES and JET. Figure 7.9 compares the BeD:Be ratios in the above mentioned experiments with our findings from publications **III** and **IV**. Therefore, this approach is able to provide a more precise database of erosion yields to the large scale impurity transport codes such as ERO [97].

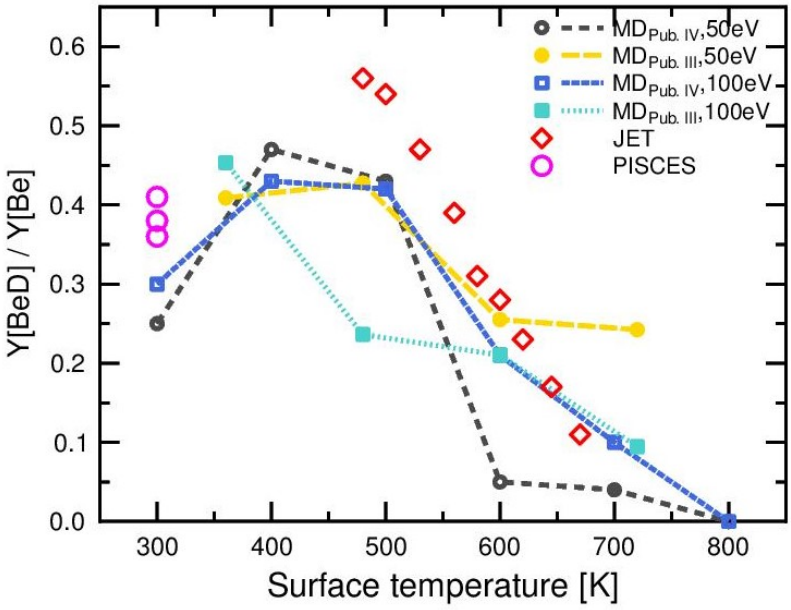

Figure 7.9: A comparison of the BeD:Be ratios obtained by two different MD approaches and experiments done at JET and PISCES as a function of the surface temperature. From publications III and IV.

Chapter 8

Summary

In this dissertation, the plasma surface interactions expected in the first wall of a fusion reactor have been investigated by several atomistic simulation methods.

First, the viability of iron-based alloys for steel as wall material was studied. The surface erosion and morphology changes due to deuterium irradiation were investigated. Fe sputtering yield had a positive correlation with impact energy, while the effect of substrate temperature for the surfaces studied here was negligible. In iron carbide, because of C preferential sputtering during the irradiation, the surface was enriched with Fe. Analysing the sputtering mechanism of Fe and C showed that at lower impact energies, the sputtering mechanism was of both physical and chemical origin while at energies higher than 100 eV, the physical sputtering dominated. Furthermore, the initial lattice structure was observed to become completely amorphised at the D implantation zone, and the trapped D in iron-based carbon-containing alloys was found to form D_2 molecules. In general, we found that if steels are used as plasma-facing material, the existence of C in them will lead to chemical sputtering. C transport and inventory calculations are therefore needed to quantify the amount of C in reactor.

The effect of plasma impurity co-bombardment (D, Ar and Ne) on sputtering and surface morphology of W and Be was also studied. Special attention was paid to the magnitude of W and Be erosion yields due to the existence and varying the fraction of irradiated Ar and Ne impurities. Overall, W and Be sputtering yields were higher in the presence of Ar and Ne plasma impurities in comparison with pure D ion irradiation, and its magnitude increased with increasing impact energy, while the effect of substrate temperatures for the surfaces studied here was negligible. However, noble gases affect significantly the total erosion of both W and Be targets at impact energies higher than 100 eV, where physical sputtering is possible. In both materials, after a few hundred bombardments the sample surface was damaged, and cell structures had changed from crystalline to amorphous at lower ion energy, and blistering-like effect was observed due to D_2 accumulation in Be cells at higher energies.

The main part of this dissertation concerned the effect of reactor-relevant parameters on Be erosion and surface morphology. For that purpose, the study was started with a cumulative D irradiation on Be by MD, scanning over different parameters. We found that the D implantation

and Be surface morphology varied greatly with temperature. The molecular erosion showed a strong dependence on the topmost surface D concentration. The simulated temperature dependence of the BeD release was in agreement with experiments performed at JET, which showed a linear drop in the BeD:Be ratio, i.e., Be sputtered as BeD, with increasing temperature in the range of 500–700 K. However, due to very different D surface contents at different temperatures, large amounts of BeD_2 and BeD_3 molecules were emitted, where these results were non-physical for reactor-like conditions, caused by the MD limitation in time. Therefore, we designed a KMC-MD multi-scale approach to investigate Be erosion in an equilibrated surface that the KMC outcome provides initial substrate structures for MD closer to experimental conditions. KMC simulations provided a D surface concentration profile for any surface temperature and incoming D energy. The results revealed a strong dependence of the D surface content on temperature. Increasing the surface temperature leads to a lower D concentration at the surface, because of the tendency of D atoms to avoid being accommodated in a vacancy, and de-trapping from impurity sites and hence diffuse fast toward bulk. At the next step, the KMC D profile was implemented as a starting configuration in MD simulations, and then total and molecular Be erosion yields due to D irradiation were analysed. Increasing the temperature and impact energy was found to decrease the fraction of Be atoms that were sputtered as BeD molecules due to the lower D surface concentrations at higher temperatures. These findings correlate well with different experiments performed at the JET and PISCES-B devices.

The mechanisms and processes identified during this dissertation improve the understanding of plasma surface interactions, such as erosion and implantation and their effect on the fusion reactor main wall. The database obtained from this work is helpful for gaining insight on the erosion and re-deposition, along with emission profile and chemical erosion of molecules, which are then accurately modelled by larger scale codes such as ERO calculations. It is therefore necessary to continue with the atomistic simulation of plasma-facing materials, scanning over different and wider parameter ranges, together with and in comparison to other modelling methods and experiments.

Acknowledgments

I wish to thank the former head of the Department of Physics at the University of Helsinki, Prof. Juhani Keinonen, and the current head, Prof. Hannu Koskinen, as well as the head of the Accelerator Laboratory, Prof. Jyrki Räisänen, for providing the facilities for the research presented in this thesis. Financial support from the EFDA, TEKES-EURATOM and the MATRENA are greatly appreciated.

I'm deeply grateful to my supervisor, Prof. Kai Nordlund, for the motivation and positive attitude. Thank you for providing both support and freedom, and a wonderful atmosphere in which to work. From you I have learned a lot. I am also thankful to Dr. Carolina Björkas and Dr. Ane Lasa for your guidance, effort and determination for a well done work and fruitful discussions.

I would also like to thank my colleagues and friends at the lab that make the lab far more than a working place. Thank you Jussi for your unconditional help and friendship and for always being there for me; Antti for your calm attitude and answering any question with your smile anytime I asked. I also would like to thank my office-mates during the last four years; Caro, Ane, Jussi, Alma, Andrea and Junlei.

My time in Finland has been far from student life. I am truly thankful to all my friends specially Hilal for her unconditional support. I wish to thank my parents and my brothers for their love, trust, motivating me and unlimited support during my whole life and even from thousands kilometres away.

Helsinki, October 24th, 2017

تقدیم به پدر بزرگوار و مادر مهربانم

آن دو فرشته ای که از خواسته هایشان گذشتند، سختی ها را به جان خریدند و خود را سپر بلای مشکلات و ناملایمات کردند تا من به جایگاهی که اکنون در آن ایستاده ام برسم

هلسینکی, ۲ آبان ۱۳۹۶

Bibliography

[1] International Energy Agency. Key World Energy Statistics. *www.iea.org/publications/freepublications/publication/KeyWorld2016.pdf*.

[2] Burn An energy journal. The connection between greenhouse gases, climate change, and global warning. *www.burnanenergyjournal.com/the-connection-between greenhouse-gases-climate-change-and-global-warming.*

[3] Paul Mobbs The Free Rang Network. Renewable energy, the potential and the limitations. *www.fraw.org.uk/mei/archive/handouts/e-series/e04/e04-renewable-energy.html.*

[4] The Joint European Torus. *www.jet.efda.org.*

[5] D-T Fusion. Science learning. *www.legacy.sciencelearn.org.nz/Contexts/Gases-and-Plasmas/Sci-Media/Images/D-T-fusion*.

[6] W. J. Nuttall. Fusion as an energy source: Challenges and opportunities. *Institute of Physics: Report*, 2008.

[7] ITER Physics Basis Editors and ITER Physics Expert Group Chairs and Co-Chairs and ITER Joint Central Team and Physics Integration Unit. Iter physics basis. *Nuclear Fusion*, 39:2137–2638, 1999.

[8] D. Kh. Morozov, E. O. Baranova, and I. Yu. Senichenkov. Impurity radiation from a tokamak plasma. *Plasma Physics Report*, 22:906–922, 2007.

[9] D. J. Ward and S. L. Dudarev. Economically competitive fusion. *Materials Today*, 11(12):46, 2008.

[10] R. A. Pitts, S. Carpentier, F. Escourbiac, T. Hirai, V. Komarov, S. Lisgo, A. S. Kukushkin, A. Loarte, M. Merola, A. Sashala Naik, R. Mitteau, M. Sugihara, B. Bazylev, and P. C. Stangeby. A full tungsten divertor for ITER: Physics issues and design status. *Journal of Nuclear Materials*, 438:S48–S56, July 2013.

[11] G. Federici. Plasma wall interactions in ITER. *Physica Scripta Volume T*, 124:1–8, May 2006.

[12] Preparing For ITER and Developing DEMO *https://www.euro-fusion.org/programme/*.

[13] G. Janeschitz, ITER JCT, and HTs. Plasma-wall interaction issues in iter. *Journal of Nuclear Materials*, 290-293:1–11, 2001.

[14] A. W. Kleyn, N. J. Lopez Cardazo, and U. Samm. Plasma-surcace interaction in the context of iter. *Physical Chemistry Chemical Physics*, 8:1761–1774, 2006.

[15] Rainer Behrisch. Plasma-facing materials for fusion devices. *Journal of Surface Investigation. X-ray, Synchrotron and Neutron Techniques*, 4(4):549–562, 2010.

[16] *The ITER Organization* http://www.iter.org/.

[17] T. N. Todd and C. G. Windsor. Progress in magnetic confinement fusion research. *Contemporary Physics*, 39(4):255–282, 1998.

[18] B J Green, ITER International Team, and Participant Teams. Iter: burning plasma physics experiment. *Plasma Physics and Controlled Fusion*, 45(5):687, 2003.

[19] et. al. B. Lipschultz. Plasma–surface interaction, scrape-off layer and divertor physics: implications for iter. *Nuclear Fusion*, 47(9):1189, 2007.

[20] G F Matthews, M Beurskens, S Brezinsek, M Groth, E Joffrin, A Loving, M Kear, M-L Mayoral, R Neu, P Prior, V Riccardo, F Rimini, M Rubel, G Sips, E Villedieu, P de Vries, M L Watkins, and EFDA-JET contributors. Jet iter-like wall—overview and experimental programme. *Physica Scripta*, 2011(T145):014001, 2011.

[21] et. al. J. Roth. Recent analysis of key plasma wall interactions issues for {ITER}. *Journal of Nuclear Materials*, 390–391:1 – 9, 2009. Proceedings of the 18th International Conference on Plasma-Surface Interactions in Controlled Fusion DeviceProceedings of the 18th International Conference on Plasma-Surface Interactions in Controlled Fusion Device.

[22] V Philipps, P Wienhold, A Kirschner, and M Rubel. Erosion and redeposition of wall material in controlled fusion devices. *Vacuum*, 67(3–4):399 – 408, 2002. 7th European Vacuum Meeting/3rd European Topical Conference on Hard Coatings.

[23] Steven J. Zinkle. Challenges in developing materials for fusion technology - past, present and future. *Fusion Science and Technology*, 64(2):65–75, 2013.

[24] S. Brezinsek, T. Loarer, V. Philipps, H.G. Esser, S. Grünhagen, R. Smith, R. Felton, J. Banks, P. Belo, A. Boboc, J. Bucalossi, M. Clever, J.W. Coenen, I. Coffey, S. Devaux, D. Douai, M. Freisinger, D. Frigione, M. Groth, A. Huber, J. Hobirk, S. Jachmich, S. Knipe, K. Krieger, U. Kruezi, S. Marsen, G.F. Matthews, A.G. Meigs, F. Nave, I. Nunes, R. Neu, J. Roth, M.F. Stamp, S. Vartanian, U. Samm, and JET EFDA contributors. Fuel retention studies with the iter-like wall in jet. *Nuclear Fusion*, 53(8):083023, 2013.

[25] G. De Temmerman, M.J. Baldwin, R.P. Doerner, D. Nishijima, and K. Schmid. An empirical scaling for deuterium retention in co-deposited beryllium layers. *Nuclear Fusion*, 48(7):075008, 2008.

[26] K. Nordlund, N. Runeberg, and D. Sundholm. Repulsive interatomic potentials calculated using Hartree-Fock and density-functional theory methods. *Nucl. Instr. Meth. Phys. Res. B*, 132:45–54, 1997.

[27] Gary S. Was. Springer Berlin Heidelberg, 2007.

[28] J. Lindhard, M. Scharff, and H. E. Schiøtt. Range concepts and heavy ion ranges. *Kgl. Danske Vid. Selskab, Mat.- Fys. Medd.*, 33 (14):1–42, 1963.

[29] H. Bethe. Zur theorie des durchgangs schneller korpuskularstrahlen durch materie. *Annalen der Physik*, 397(3):325–400, 1930.

[30] J. F. Ziegler. Stopping of energetic light ions in elemental matter. *J. Appl. Phys.*, 85(3):1249, 1999.

[31] J. F. Ziegler, J. P. Biersack, and U. Littmark. *The Stopping and Range of Ions in Matter*. Pergamon, New York, 1985.

[32] Werner Brandt and M. Kitagawa. Effective stopping-power charges of swift ions in condensed matter. *Phys. Rev. B*, 25(9):5631, 1982.

[33] J. F. Ziegler, J. P. Biersack, and M. D. Ziegler. *SRIM - The Stopping and Range of Ions in Matter*. SRIM Co., Chester, Maryland, USA, 2008.

[34] J. F. Ziegler. SRIM-2013 software package, available online at *http://www.srim.org*.

[35] K. Nordlund. Energy loss of energetic ions , available at *http://beam.helsinki.fi/ knordlun/mdh/rangetext.html*.

[36] R.A. Anderl, R.A. Causey, J.W. Davis, R.P. Doerner, G. Federici, A.A. Haasz, G.R. Longhurst, W.R. Wampler, and K.L. Wilson. Hydrogen isotope retention in beryllium for tokamak plasma-facing applications. *Journal of Nuclear Materials*, 273(1):1 – 26, 1999.

[37] J.B. Condon and T. Schober. Hydrogen bubbles in metals. *Journal of Nuclear Materials*, 207:1 – 24, 1993.

[38] C. H. Skinner, A. A. Haasz, V. Kh. Alimov, N. Bekris, R. A. Causey, R. E. H. Clark, J. P. Coad, J. W. Davis, R. P. Doerner, M. Mayer, A. Pisarev, J. Roth, and T. Tanabe. Recent advances on hydrogen retention in iter's plasma-facing materials: Beryllium, carbon, and tungsten. *Fusion Science and Technology*, 54(4):891–945, 2008.

[39] C.H. Wu and North Atlantic Treaty Organization. Scientific Affairs Division. *Hydrogen Recycling at Plasma Facing Materials*. NATO science series: Mathematics, physics, and chemistry. Springer Netherlands, 2000.

[40] J. Roth. *Review and Status of Physical Sputtering and Chemical Erosion of Plasma Facing Materials*, pages 203–224. Springer Berlin Heidelberg, Berlin, Heidelberg, 2005.

[41] R. Behrisch and W. Eckstein (ed.). *Sputtering by Particle Bombardment: Experiments and Computer Calculations from Threshold to MeV Energies*. Springer, Berlin, 2007.

[42] P. Sigmund. Mechanisms and theory of physical sputtering by particle impact. *Nucl. Instr. Meth. Phys. Res. B*, 27:1, 1987.

[43] M. T. Robinson and Ian M. Torrens. Computer simulation of atomic-displacement cascades in solids in the binary-collision approximation. *Phys. Rev. B*, 9(12):5008, 1974.

[44] Dirk Naujoks. *Plasma-material interaction in controlled fusion*, volume 39. Springer Science & Business Media, 2006.

[45] K. Nordlund, E. Salonen, A. V. Krasheninnikov, and J. Keinonen. Swift chemical sputtering of covalently bonded materials. *Pure and Applied Chemistry*, 78(6):1203–1212, 2006.

[46] C. Björkas, K. Vörtler, K. Nordlund, D. Nishijima, and R. Doerner. Chemical sputtering of be due to d bombardment. *New Journal of Physics*, 11:123017, 2009.

[47] Rainer Behrisch and K Wittmaack. *Sputtering by particle bombardment*, volume 1. Springer Berlin, 1981.

[48] YU. V. Martynenko. The theory of blister formation. *Radiation Effects*, 45(1-2):93–101, 1979.

[49] B. J. Alder and T. E. Wainwright. Studies in Molecular Dynamics. I. General Method. *J. of Chem. Phys.*, 31(2):459, 1959.

[50] M. P. Allen and D. J. Tildesley. *Computer Simulation of Liquids*. Oxford University Press, Oxford, England, 1989.

[51] K. Nordlund, 2016. PARCAS computer code. The main principles of the molecular dynamics algorithms are presented in [**?** **?**]. The adaptive time step and electronic stopping algorithms are the same as in [**?**]. The 2016 version of the code is published in the supplementary material to Ref. [**?**].

[52] H. J. C. Berendsen, J. P. M. Postma, W. F. van Gunsteren, A. DiNola, and J. R. Haak. Molecular dynamics with coupling to external bath. *J. Chem. Phys.*, 81(8):3684, 1984.

[53] J. Tersoff. New Empirical approach for the structure and energy of covalent systems. *Phys. Rev. B*, 37:6991, 1988.

[54] Donald W. Brenner. Empirical potential for hydrocarbons for use in simulating the chemical vapor deposition of diamond films. *Phys. Rev. B*, 42(15):9458, 1990. ; *idem*, 46, 1948 (1992).

[55] M. W. Finnis and J. E. Sinclair. A simple empirical N-body potential for transition metals. *Phil. Mag. A*, 50(1):45, 1984. *see also Erratum, ibid. 53 (1986) 161*.

[56] Fabrizio Cleri and Vittorio Rosato. Tight-binding potentials for transition metals and alloys. *Phys. Rev. B*, 48:22–33, Jul 1993.

[57] Karsten Albe, Kai Nordlund, and Robert S. Averback. Modeling the metal-semiconductor interaction: Analytical bond-order potential for platinum-carbon. *Phys. Rev. B*, 65:195124, May 2002.

[58] N. Juslin, P. Erhart, P. Träskelin, J. Nord, K. O. E. Henriksson, K. Nordlund, E. Salonen, and K. Albe. Analytical interatomic potential for modelling non-equilibrium processes in the W-C-H system. *J. Appl. Phys.*, 98:123520, 2005.

[59] C. Björkas, N. Juslin, H. Timko, K. Vörtler, K. Henriksson, K. Nordlund, and P. Erhart. Interatomic potentials for be, be-c and be-h. *Journal of Physics: Condensed Matter*, 21:445002, 2009.

[60] Pekko Kuopanportti, Erin Hayward, Chu-Chun Fu, Antti Kuronen, and Kai Nordlund. Interatomic fe-h potential for irradiation and embrittlement simulations. *Computational Materials Science*, 111:525 – 531, 2016.

[61] K. O. E. Henriksson, C. Björkas, and K. Nordlund. Enabling atomistic simulations of stainless steels: A bond-order potential for Fe-Cr-C system. *J. Phys. Condens. Matt.*, 25(44):445401, 2013.

[62] Murray S. Daw, Stephen M. Foiles, and Micael I. Baskes. The embedded-atom method: a review of theory and applications. *Mat. Sci. Rep.*, 9:251, 1993.

[63] N. W. Ashcroft and N. D. Mermin. *Solid State Physics*. Saunders College, Philadelphia, 1976.

[64] R. Smith (ed.). *Atomic & ion collisions in solids and at surfaces: theory, simulation and applications*. Cambridge University Prss, Cambridge, UK, 1997.

[65] J. F. Ziegler, 1992. TRIM-92 computer code, private communication.

[66] W. Möller and W. Eckstein. TRIDYN - a TRIM simulation code including dynamic composition changes. *Nucl. Instr. Meth. Phys. Res. B*, 2:814–818, 1984.

[67] W. Eckstein. *Computer Simulations of Ion-Solid Interactions*. Springer, Berlin, 1991. p. 40.

[68] W. Eckstein, R. Dohmen, A. Mutzke, and R. Schneider. SDTrimSP: A Monte-Carlo Code for Calculating Collision Phenomena in Randomized Targets. 2007.

[69] N. Metropolis and S. Ulam. The Monte Carlo Method. *J. Amer. Stat. Assoc*, 44, 1949. 335.

[70] K. A. Fichthorn and W. H. Weinberg. Theoretical foundations of dynamical Monte Carlo simulations. *J. Chem. Phys*, 95(2):1090, 1991.

[71] H. T. MacGillivray and R. J. Dodd. Monte-carlo simulations of galaxy systems. *Astrophysics and Space Science*, 86(2):437–452, 1982.

[72] J.W. Tringe, N. Ileri, H.W. Levie, P. Stroeve, V. Ustach, R. Faller, and P. Renaud. Molecular dynamics and monte carlo simulations resolve apparent diffusion rate differences for proteins confined in nanochannels. *Chemical Physics*, 457:19 – 27, 2015.

[73] A. Kirschner, V. Philipps, J. Winter, and U. Kögler. Simulation of the plasma-wall interaction in a tokamak with the monte carlo code ero-textor. *Nuclear Fusion*, 40(5):989, 2000.

[74] G. Kresse *et al.* Ab initio molecular dynamics for liquid metals. *Phys. Rev. B*, 47:558, 1993. *ibid.,* Phys. Rev. B, 49 (1994) 14251; Comput. Mat. Sci., 6 (1996) 15; Phys. Rev. B, 54 (1996) 11169.

[75] C S Becquart, M F Barthe, and A De Backer. Modelling radiation damage and he production in tungsten. *Physica Scripta*, 2011(T145):014048, 2011.

[76] C. S. Becquart and C. Domain. Modeling microstructure and irradiation effects. *Metallurgical and Materials Transactions A*, 42(4):852–870, 2011.

[77] A. B. Bortz, M. H. Kalos, and J. L. Lebowitz. A new algorithm for Monte Carlo Simulation of Ising Spin Systems. *J. Computational Physics*, 17:10–18, 1975.

[78] Arthur F. Voter. *INTRODUCTION TO THE KINETIC MONTE CARLO METHOD*, pages 1–23. Springer Netherlands, Dordrecht, 2007.

[79] D.P. Landau and K. Binder. *A Guide to Monte Carlo Simulations in Statistical Physics*. Cambridge University Press, 2000.

[80] Ignacio Martin-Bragado, Antonio Rivera, Gonzalo Valles, Jose Luis Gomez-Selles, and María J. Caturla. Mmonca: An object kinetic monte carlo simulator for damage irradiation evolution and defect diffusion. *Computer Physics Communications*, 184(12):2703 – 2710, 2013.

[81] G. Valles, C. González, I. Martin-Bragado, R. Iglesias, J.M. Perlado, and A. Rivera. The influence of high grain boundary density on helium retention in tungsten. *Journal of Nuclear Materials*, 457:80 – 87, 2015.

[82] R. Behrisch, J. Roth, J. Bohdansky, A.P. Martinelli, B. Schweer, D. Rusbüldt, and E. Hintz. Dependence of light-ion sputtering yields of iron on ion fluence and oxygen partial pressure. *Journal of Nuclear Materials*, 93:645 – 655, 1980.

[83] J. Bohdansky, J. Roth, and H. L. Bay. Erratum:An analytical formula and important parameters for low-energy ion sputtering [J. Appl. Phys. 51, 2861 (1980)]. *Journal of Applied Physics*, 52:1610, March 1981.

[84] K. O. E. Henriksson and K. Nordlund. Mechanical and elastic changes in cementite Fe3C subjected to cumulative 1 keV Fe recoils. *Nucl. Instr. Meth. Phys. Res. B*, 338:119, 2014.

[85] K. Vörtler, C. Björkas, and K. Nordlund. The effect of plasma impurities on the sputtering of tungsten carbide. *J. Phys.: Conden. Matter*, 23(8):085002, 2010.

[86] A Kreter, T Dittmar, D Nishijima, R P Doerner, M J Baldwin, and K Schmid. Erosion, formation of deposited layers and fuel retention for beryllium under the influence of plasma impurities. *Physica Scripta*, 2014(T159):014039, 2014.

[87] R. Parker, G. Janeschitz, H.D. Pacher, D. Post, S. Chiocchio, G. Federici, P. Ladd, ITER Joint Central Team, and Home Teams. Plasma-wall interactions in iter. *Journal fo Nuclear Materials*, 241-243:1–26, 1997.

[88] A. Kallenbach, M. Balden, R. Dux, T. Eich, C. Giroud, A. Huber, G.P. Maddison, M. Mayer, K. McCormick, R. Neu, T.W. Petrie, T. Pütterich, J. Rapp, M.L. Reinke, K. Schmid, J. Schweinzer, and S. Wolfe. Plasma surface interactions in impurity seeded plasmas. *Journal of Nuclear Materials*, 415(1):S19 – S26, 2011. Proceedings of the 19th International Conference on Plasma-Surface Interactions in Controlled Fusion.

[89] T. Nakano, N. Asakura, and H. Kubo. Contribution of ne ions to radiation enhancement in jt-60u divertor plasmas. *Journal of Nuclear Materials*, 438:S291 – S296, 2013. Proceedings of the 20th International Conference on Plasma-Surface Interactions in Controlled Fusion Devices.

[90] M. Ishida, H.T. Lee, and Y. Ueda. The influence of neon or argon impurities on deuterium permeation in tungsten. *Journal of Nuclear Materials*, 463:1062 – 1065, 2015. PLASMA-SURFACE INTERACTIONS 21.

[91] P. Träskelin, K. Nordlund, and J. Keinonen. H, He, Ne, Ar-bombardment of amorphous hydrocarbon structures. *J. Nucl. Mater*, 357:1–8, 2006.

[92] TURBOMOLE V5.10. Turbomole GmbH. *Karlsruhe*, 2008.

[93] F. Virot, M. Barrachin, S. Souvi, and L. Cantrel. Theoretical prediction of thermodynamic properties of tritiated beryllium molecules and application to iter source term. *Fusion Engineering and Design*, 89(7):1544 – 1550, 2014. Proceedings of the 11th International Symposium on Fusion Nuclear Technology-11 (ISFNT-11) Barcelona, Spain, 15-20 September, 2013.

[94] S. Brezinsek, M.F. Stamp, D. Nishijima, D. Borodin, S. Devaux, K. Krieger, S. Marsen, M. O'Mullane, C. Bjoerkas, A. Kirschner, and JET EFDA contributors. Study of physical and chemical assisted physical sputtering of beryllium in the jet iter-like wall. *Nuclear Fusion*, 54(10):103001, 2014.

[95] A Lasa, K Schmid, and K Nordlund. Modelling of w–be mixed material sputtering under d irradiation. *Physica Scripta*, 2014(T159):014059, 2014.

[96] D. Nishijima, R.P. Doerner, M.J. Baldwin, and G. De Temmerman. Erosion yields of deposited beryllium layers. *Journal of Nuclear Materials*, 390:132 – 135, 2009. Proceedings of the 18th International Conference on Plasma-Surface Interactions in Controlled Fusion Device.

[97] A. Kirschner, V. Philipps, J. Winter, and U. Kögler. Simulation of the plasma-wall interaction in a tokamak with the monte carlo code ero-textor. *Nuclear Fusion*, 40(5):989, 2000.